2023-12-18

Local Atomic and Magnetic Structure of Multiferroic (Sr,Ba)(Mn,Ti)O3

Braedon Jones
Brigham Young University

BYU ScholarsArchive Citation

Jones, Braedon, "Local Atomic and Magnetic Structure of Multiferroic (Sr,Ba)(Mn,Ti)O3" (2023). *Theses and Dissertations*. 10243.
https://scholarsarchive.byu.edu/etd/10243

Local Atomic and Magnetic Structure of Multiferroic (Sr,Ba)(Mn,Ti)O_3

Braedon Jones

A thesis submitted to the faculty of
Brigham Young University
in partial fulfillment of the requirements for the degree of

Master of Science

Benjamin Frandsen, Chair
Richard Sandberg
Stacey Smith

Department of Physics and Astronomy

Brigham Young University

ABSTRACT

Local Atomic and Magnetic Structure of Multiferroic (Sr,Ba)(Mn,Ti)O_3

Braedon Jones
Department of Physics and Astronomy, BYU
Master of Science

We present a detailed study of the local atomic and magnetic structure of the type-I multiferroic perovskite system (Sr,Ba)(Mn,Ti)O_3 using x-ray and neutron pair distribution function (PDF) analysis, polarized neutron scattering, and muon spin relaxation (μSR) techniques. The atomic PDF analysis reveals widespread nanoscale tetragonal distortions of the crystal structure even in the paraelectric phase with average cubic symmetry, corresponding to incipient ferroelectricity in the local structure. Magnetic PDF analysis, polarized neutron scattering, and μSR likewise confirm the presence of short-range antiferromagnetic correlations in the paramagnetic state, which grow in magnitude as the temperature approaches the magnetic transition. We show that these short-range magnetic correlations coincide with a reduction of the tetragonal (i.e. ferroelectric) distortion in the average structure, suggesting that short-range magnetism can play an important role in magnetoelectric and/or magnetostructural phenomena even without genuine long-range magnetic order. The reduction of the tetragonal distortion scales linearly with the local magnetic order parameter. These findings provide greater insight into the multiferroic properties of (Sr,Ba)(Mn,Ti)O_3 and demonstrate the importance of investigating the local atomic and magnetic structure to gain a deeper understanding of the intertwined degrees of freedom in multiferroics.

Keywords: Multiferroics, Pair Distribution Function, Magnetic Pair Distribution Function

ACKNOWLEDGMENTS

I would like to thank foremost my parents and family for all of their love and support throughout the years.

Contents

Chapter 1

Multiferroics

Multiferroics are a rare but potentially significant class of materials that have been the subject of increased study over the past few decades. These materials exhibit coexistence of two or more of the classic ferroic orders: ferroelectric, ferromagnetic, and ferroelastic [1]. Ferromagnets possess a spontaneous magnetization that can be altered through an applied magnetic field [2], ferroelectrics have spontaneous electric polarization that is alterable with an applied electric field [2], and ferroelastics have a spontaneous deformation that can be modified through the application of stress [2]. A visualization of the three main ferroic orders and their possible interactions is shown in Fig 1.1. The three vertices of the triangle are labeled E, H, and σ, representing electric, magnetic, and stress fields, respectively. The inside of the triangle reads P, M, and ε indicating the three primary ferroic orders of ferroelectricity, ferromagnetism, and ferroelasticity. The cross-coupling, as shown with the black and green arrows on the figure, are what spark the growing interest in multiferroics. The coupling between electric polarization and material deformation results in piezoelectricity, which has proven useful in numerous applications, such as sonar detectors [2]. Piezomagnetism is resultant from the coupling between structure and magnetism and is used for magnetic sensing [2]. The coupling between ferroelectricity and ferromagnetism defines magnetoelectric multiferroics [2].

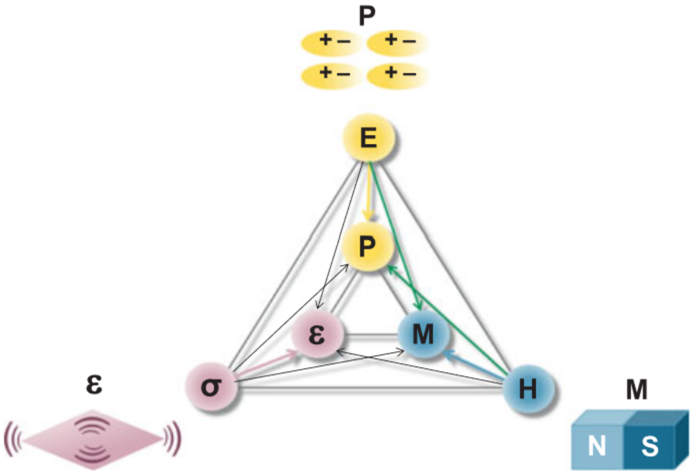

Figure 1.1 Multiferroics possess at least two of the following orders: ferroelectric (**P**), ferromagnetic (**M**), and/or ferroelastic (ε) order, as seen symbolized in the interior of the triangle. The corresponding vertices of the triangle represent the conjugate magnetic (**H**), electric (**E**), and stress (σ) fields. Adapted from Ref. [2].

1.1 Magnetoelectric Multiferroics

The scientific community is especially enamored with magnetoelectric multiferroics. Commonly, the use of the term "multiferroic" implies magnetoelectric multiferroics rather than the other possible types of multiferroics. This thesis will likewise use "multiferroic" to refer to magnetoelectric multiferroics. Such materials are rare but very appealing for their myriad potential in application. The cross-coupling allows for electrical control of magnetization or vice versa. Such an ability assists in developing smaller and more energy efficient devices, as it requires more energy to create a suitable magnetic field than an electric field. By replacing a magnetic field with an electric field to write data, the whole process becomes more energetically efficient [2]. Furthermore, a magnetic bit can be combined with an electric bit to create a four-state memory element [3]. Multiferroic bits would decrease data storage size and increase computational speed. Various other possible applications of multiferroics include AC/DC magnetic field sensors, microwave resonators tuned electrically, microwave phase shifter, microwave signal delay line, RAM and multi-state memories, photovoltaic solar cells, thermal energy harvesting, gyrators, and solid state cooling, among many other potential uses [4]. Overall, this entails a plethora of uses in energy transformation, information science, and signal processing. Study of multiferroics can have crossover effects into other research areas, such as complex magnetism and ferroelectricity, oxide heterostructures, and even cosmology [3, 5].

The knowledge of magnetism has existed for over 2,500 years, yet the discovery of spontaneous electric dipole moments in solids occurred a little over a century ago [3]. Attempts to combine these two orders first occurred only in the late 1950s, achieving limited results at that time [3, 6]. A large part of the difficulty in studying multiferroics stems from the relative rarity of such materials. This arises in consequence of the opposing atomic-scale properties that enable the desired macroscopic material behavior. First, ferroelectricity requires structural distortions that remove the center of symmetry [6]. Thirty-one point groups exist that permit spontaneous electric polarization [5]. There are also 31 points groups that allow for spontaneous magnetization [5]. Of these 31, only 13 point groups have the correct symmetries for both ferroelectricity and ferromagnetism and 8 point groups exists that allow for simultaneous ferroelectricity and antiferromagnitism [5]. This reduces, but does not all together prevent, multiferroicity. Another factor contributing to multiferroic scarcity results from ferroelectrics being insulators by definition, yet most ferromagnetic materials are metals. One of the largest factors contributing toward the dearth of multiferroics has to do with ”d^0-*ness*.” For perovskites, ferroelectricity occurs through the hybridization of the electron clouds of neighboring ions which leads to off-centered ions. This hybridization occurs through the covalent bonding and virtual hopping of electrons in a filled p-orbital with an empty d-orbital of a transition metal ion [7]. Alternatively, magnetism best occurs with a partially filled d-orbital with unpaired valence electrons, as each unpaired electron contributes a spin and thus a long range magnetic ordering.

Transition metals, with their partially filled d-orbitals, would then be expected to express magnetic properties. A fundamental contradiction persists with magnetic materials requiring a partially filled d-orbital and ferroelectric materials preferring an empty d-shell. Thus, other structural factors must contribute to overcome this inherent ordering opposition [2, 6].

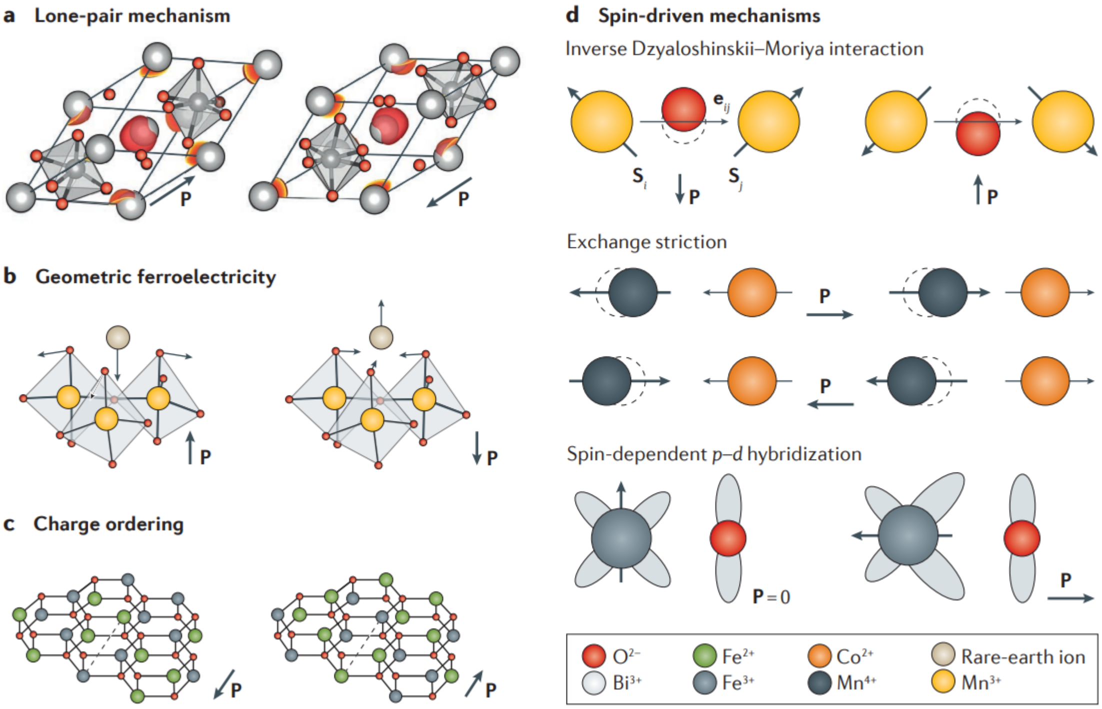

Figure 1.2 A number of structural or spin-driven mechanisms that permit for multiferroicity despite the opposition between partially filled d-valence shells for magnetic transition metals and the energetically favorable empty d-shells in connection with ferroelectricity. In **a**, two Bi^{3+} electrons shift away from the Bi^{3+} ion, leading to a spontaneous polarization. In **b**, deformation in MnO_5 bipyramids displace the rare-earth ions, resulting in electric polarization. In **c**, layering with alternating ratios of Fe^{2+} / Fe^{3+} leads to a polarization. In **d**, various spin-driven methods that yield a spontaneous polarization are shown. Spins can cause displacements through asymmetric spin exchange interactions (top panel) and symmetric spin exchanges (middle panel). Spin-driven modulations between orbitals leads to a polarization as well (bottom panel). Adapted from Ref. [3].

The occurrence of simultaneous magnetic and electric dipole moments can be caused through a variety of unconventional mechanisms as exhibited in Fig. 1.2. The lone-pair mechanism can produce ferroelectricity as a result of an anisotropic distribution of unbonded valence electrons around the ion of origin. This leads to a spontaneous polarization, but the magnetic ordering in certain materials, such as $BiFeO_3$, are associated with different ions, producing a weak coupling between orders [3, 8]. Another method is through spin-driven ferroelectricity, where spin ordering leads to ferroelectric polarization. One material that utilizes this method, $TbMnO_3$, has strong coupling between ordering parameters, but the polarization magnitude is too small for technological application [8]. Charge ordering theoretically can lead to ferroelectricity by variation in the number of valence electrons associated with each ion in the layers of the lattice. Geometric ferroelectricity is accomplished through rotational distortions that can cause structural instabilities in the lattice. These four methods are exhibited in Fig. 1.2.

Related to, but distinct from, these various mechanisms to achieve multiferroicity is the classification of multiferroics into Type-I and Type-II materials [5]. Type-I multiferroics usually have magnetic and ferroelectric transitions at widely separated temperatures, and the mechanism for such order is fairly independent of one another, as exemplified by $BiFeO_3$. These materials frequently offer technologically favorable electric polarization magnitudes and ordering temperatures, but cross-order control is limited due to the weak coupling between the orders. Type-II materials differ in that there is a magnetically-driven ferroelectric transition, so that there is a strong link between the two orders, as seen in $TbMnO_3$. However, the polarization magnitude is usually weaker and restricted to lower temperature ranges, limiting potential technological application. In the realm of multiferroics, a major goal is to discover or engineer materials that exhibit the positive traits of both Type-I and Type-II [9]. This would involve materials with strong linking between ferroelectric and magnetic orders, high polarization magnitudes, and ordering temperatures occurring in applicable ranges. To accomplish such an endeavor, preliminary steps require a more complete understanding of magnetoelectric coupling in representative systems. Fortunately, recent developments in theory, synthesis, and characterization, including at atomic and nanoscale levels, provide exciting new opportunities to study multiferroic materials and advance their potential technological application for societal benefit.

1.2 Outline of this Thesis

This thesis will focus on the magnetoelectric multiferroic material (Sr,Ba)(Mn,Ti)O_3. After an overview of this system, including its reported behavior around transition temperatures, we will report the experimental methods used in this thesis project, including atomic and magnetic pair distribution function analysis and muon spin spectroscopy. We will then describe the experimental results and data analysis, which reveal significant local symmetry breaking and short-range magnetic correlations over a wide temperature range. We then discuss the significance of these results, including the finding of linear magnetoelectric coupling involving short-range magnetic correlations, and then finally conclude with an outlook regarding next steps and potential applications.

The bulk of this thesis forms a manuscript that is currently under review at *Physics Review B*. The full bibliographic information is as follows: Braedon Jones, Christiana Z. Suggs, Elena Krivyakina, Daniel P. Phelan, V. Ovidiu Garlea, Omar Chmaissem, and Benjamin A. Frandsen; "Local atomic and magnetic structure of multiferroic (Sr,Ba)(Mn,Ti)O_3". As the lead student author, I carried out the majority of the experiments, data analysis, and writing, under the supervision of my advisor Ben Frandsen and with input from all coauthors on the paper. More specifically, in the course of my master's research, I performed x-ray diffraction on powder samples, carried out neutron pair distribution function experiments, analyzed the neutron and x-ray pair distribution function data, performed fits to the atomic and magnetic pair distribution function data, analyzed the polarized neutron scattering data, and coordinated the efforts to incorporate all of the data and results into the manuscript. The samples were synthesized by Elena Krivyakina and Dr. Omar Chmaissem. Magnetic susceptibility measurements were performed by Dr. Daniel Phelan. The polarized neutron scattering experiments were performed by Dr. Ovi Garlea, as well as some of the magnetic diffraction analysis. Christiana Zaugg was the student lead for the μSR portion of this work. All images in this thesis were provided by myself, unless otherwise noted.

Chapter 2

(Sr,Ba)(Mn,Ti)O_3

2.1 Character and Behavior

In the search for multiferroic materials that combine the best traits of both Type-I and Type-II materials, the perovskite material (Sr,Ba)MnO_3 has recently attracted interest as a promising system [8,10–14]. It is a Type-I multiferroic with a relatively large electric polarization of $\sim$4.5 μC/cm^2, yet the ferroelectric (FE) and antiferromagnetic (AFM) orders are strongly coupled in a manner similar to prototypical type-II multiferroics. This material, in contrast to the previous discussion on ferromagnetic multiferroics, is an antiferromagnetic multiferroic. This implies some technological limitations in application in comparison to ferromagnetic multiferroics, but nevertheless this material still can build a foundation for understanding the mechanisms of multiferroic coupling.

The unusually strong magnetoelectric coupling of (Sr,Ba)MnO_3 is understood as a consequence of the Mn sublattice being responsible for both the electric polarization and the magnetic order, providing a unique route to outstanding multiferroic properties in (Sr,Ba)MnO_3 [8]. The Mn^{4+}

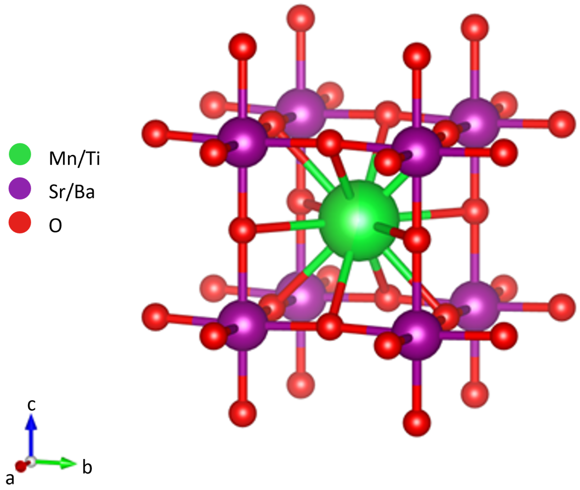

Figure 2.1 Cubic structure of (Sr,Ba)MnO_3, visualized with the program Vesta [15]. The center green atomic site represents either Mn or Ti and is the site of the cause of both the antiferromagnetic and ferroelectric ordering. The purple spheres represent Sr or Ba, while the red spheres represent the oxygen sites. As the temperature is lowered below the ferroelectric Curie temperature, the structure distorts into tetragonal symmetry.

position leads to ferroelectricity, while below the Nèel temperature, the spins localized on the Mn^{4+} sites order in an antiferromagnetic orientation. This coupling mechanism is related to the spin-driven exchange striction as discussed previously.

In the paraelectric state, (Sr,Ba)MnO_3 adopts the typical cubic perovskite structure, as shown in Fig. 2.1. The FE transition around 400 K is associated with an off-centering displacement of the Mn^{4+} ion relative to the surrounding O^{2-} ions and a tetragonal distortion, in which c becomes slightly greater than a. The resulting space group is $P4mm$ [13]. Below approximately 200 K, G-type AFM order develops, characterized by anti-parallel alignment between nearest-neighbor Mn^{4+} spins. The magnetic space group was previously reported as $P4/m'm'm$ [13]. The onset of magnetic order coincides with a significant reduction of the tetragonal (and therefore ferroelectric) distortion to about 30% of the maximum distortion, demonstrating strong magnetoelectric coupling.

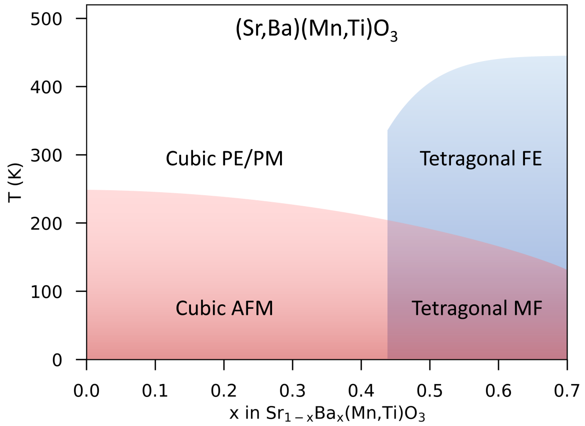

Figure 2.2 Phase diagram for $Sr_{1-x}Ba_xMn_{1-y}Ti_yO_3$ as a function of temperature and barium content x. Compositions with $x \geq 0.5$ are synthesized with dilute amounts of Ti on the Mn site. Compiled by Dr. Frandsen from results published in Refs. [8, 13, 14]. PE = paraelectric; PM = paramagnetic; FE = ferroelectric; AFM = antiferromagnetic; MF = multiferroic.

Interestingly, this reduction of the FE distortion begins nearly 100 K above T_N and grows as the temperature approaches the magnetic transition. It has been speculated, though not shown, that short-range magnetic correlations in the paramagnetic state are responsible for this behavior [8, 11].

The FE and AFM ordering temperatures can be tuned by varying the Ba content in $Sr_{1-x}Ba_xMnO_3$. Ferroelectricity first appears for $x = 0.43$ with a Curie temperature of $T_C = 330$ K, which rises rapidly to about 400 K for $x = 0.5$. Ba content beyond $x = 0.5$ can be stabilized by co-substitution with small amounts of Ti on the Mn site [14], with a maximum Ba content of $x = 0.7$ achievable with a Ti content of $y = 0.12$ in $Sr_{1-x}Ba_xMn_{1-y}Ti_yO_3$. T_C increases slightly to approximately 430 K for the largest Ba concentrations. Meanwhile, the Néel temperature T_N decreases from 200 K for $x = 0.43$ to approximately 130 K for $x = 0.7$ [14]. The phase diagram in the space of temperature versus Ba content is given in Fig. 2.2.

2.2 Previous Studies of (Sr,Ba)(Mn,Ti)O_3

Several studies have been conducted to characterize the ferroelectric and magnetic properties in (Sr,Ba)(Mn,Ti)O_3 [8,10–14]. In two separate studies utilizing x-ray diffraction, the average, long-range structure was seen to undergo a tetragonal lattice distortion. This distortion causes the ferroelectric behavior of $Sr_{1-x}Ba_xMnO_3$. The left diffraction pattern in Fig. 2.3 shows a splitting of the (002) and (200) peaks, which are equivalent in the ideal cubic structure but distinct in the tetragonal structure. This splitting is observed primarily between the Curie (305 K for this particular composition) and Néel temperatures. As the temperature decreases towards the Néel temperature, the distortion diminishes markedly. This points to a coupling between the orders, with the reduction of the tetragonal distortion appearing as a consequence of the onset of the magnetic order. The right panel in Fig. 2.3 shows three different diffraction patterns for three different compositions of $Sr_{1-x}Ba_xMnO_3$, with x = 0.43, 0.44, and 0.45, as synthesized through a well established stoichiometric procedure and with oxygen content verified through thermogravimetric analysis. X-ray and neutron diffraction thereafter confirmed phase purity. The tetragonal (i.e. ferroelectric) distortion is visible for the $x = 0.43$ compound only as a faint broadening of the diffraction peak between about 300 and 200 K, indicating a very small tetragonal distortion. With increasing Ba content, the tetragonal distortion becomes larger, as evidenced by the larger splitting of the diffraction peaks, and is stabilized over a wider temperature interval.

Structural studies of the tetragonal distortion are relevant to the ferroelectric properties because the net electric dipole moment can be calculated from the structural parameters of the tetragonal unit cell. The relevant parameters include the two distinct Mn-O1 bond lengths, the Mn-O2 bond length, and the Mn-O2-Mn bond angle. The dipole moment is calculated as

$$|P| = q[\Delta[Mn-O1] + (4 \times [Mn-O2] \times \sin(\frac{180^{\circ} - <Mn-O2-Mn>}{2}))] \tag{2.1}$$

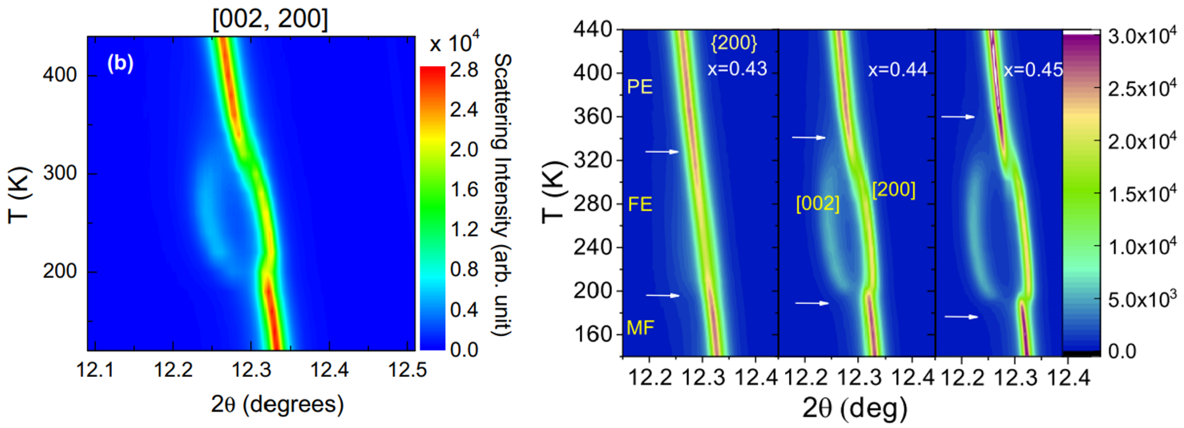

Figure 2.3 X-ray powder diffraction data taken for Sr$_{1-x}$Ba$_x$MnO$_3$ with a Ba content of x = 0.44 in the left image and a variety of Ba compositions in the right figure [11, 13]. At temperatures below T$_C$, a tetragonal distortion is evident. This distortion is partially suppressed below T_N. For Barium content of $x = 0.44$ and $x = 0.45$ in the right hand figure, the distortion is more pronounced than for $x = 0.43$.

with $q = 1.95e$, where e is the fundamental electron charge [13]. These structural parameter values may be acquired through Rietveld refinement of x-ray or neutron diffraction data or through pair distribution function (PDF) fits. As specified by the equation, a greater net polarization will occur with a larger difference between the Mn-O1 lengths, which scales with the magnitude of the tetragonal distortion.

The coupling between the antiferromagnetic and ferroelectric orders causes the tetragonal structure distortion to diminish as temperatures decreases, although the structure never returns to a full cubic structure, as a slight difference in a and c lattice parameters remains at all temperatures below the Néel transition. The suppression of the tetragonal distortion occurs higher than the Néel temperature, as noted from Rietveld refinements of diffraction data shown in Fig. 2.4, where around 250 K, the c value starts to decline [13]. Furthermore, as seen on the right panel of Fig. 2.4, the dielectric permittivity as a function of temperature obtained from broadband spectroscopy

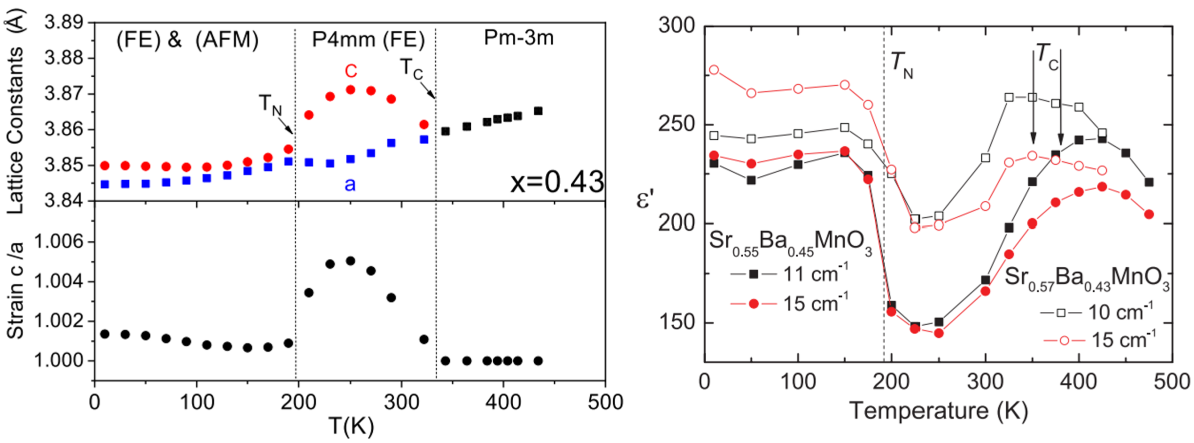

Figure 2.4 The splitting in *c* and *a* lattice parameter lengths occurs below T_C, but, because of the coupling to the antiferromagnetic order, they converge as the magnetic order develops. The convergence begins above T_N, suggesting that short-range magnetic correlations drive these changes in the average structure. Similar early convergence is demonstrated in the right graph of dielectric permittivity as a function of temperature [12, 13].

experiments likewise shows a response at temperatures well above T_N [12]. The fact that the magnetoelectric coupling manifests at temperature far above the long-range magnetic ordering temperature suggests that the coupling may be facilitated by short-range magnetic correlations that exist in the paramagnetic state. If the magnetoelectric coupling were to depend entirely on long-range magnetic correlations, then the reduction of the tetragonal distortion would not be expected until below T_N. However, experimental data sensitive to short-range magnetic and structural correlations has not been available to this point. A study into the local structure of $Sr_{1-x}Ba_xMnO_3$ would reveal possible short-range magnetic correlations that could contribute to the macroscopically observed reduction of the tetragonal distortion, and thus the diminished ferroelectricity.

‘

Chapter 3

Methods

3.1 Atomic and Magnetic Pair Distribution Function Analysis

Features of the local structure such as short-range structural correlations that differ from the long-range crystallographic structure have long been recognized as crucial for understanding ferroelectric materials. For example, short-range tetragonal distortions resulting in local polar displacements within an average centrosymmetric crystal structure have been observed in numerous perovskite-based ferroelectrics ranging from classic systems such as $BaTiO_3$ to complex relaxor ferroelectrics [16–20]. The presence and evolution of such short-range ferroelectric distortions have yielded insights into the transition mechanism and origin of the observed ferroelectric behavior. Many of these local-structure studies have utilized pair distribution function (PDF) analysis of x-ray and neutron total scattering data, one of the most powerful methods available for quantitatively elucidating local atomic structure [21]. By Fourier transforming the total scattering signal, which includes both the Bragg peaks arising from the average crystal structure and the diffuse scattering from local deviations from the average structure, the PDF provides a real-space view of the local

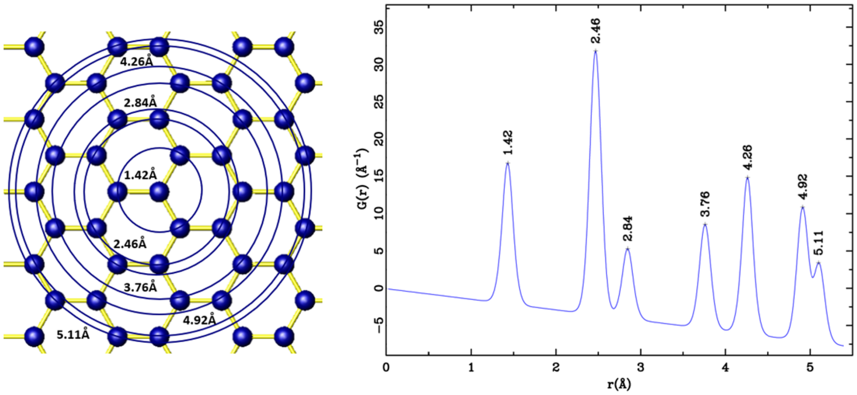

Figure 3.1 Example PDF pattern (right panel) calculated from the hexagonal crystal structure shown on the left. From [25].

structure in the form of a histogram of interatomic distances on length scales ranging from nearest-neighbor distances of Ångstroms to several nanometers or longer. The PDF method has had a major impact on structural studies of functional materials, quantum materials, and more [22–24].

An example PDF generated from a honey-comb crystal is shown in Fig. 3.1. The concentric rings overlaid on the crystal structure on the left show the near-neighbor distances from the central atom for each subsequent coordination shell of atoms. These interatomic distances correspond to the peaks in the PDF plot on the right. Some rings possess more atoms, leading to higher peaks, since peak height scales with the probability of finding a pair of atoms separated by the given distance [25]. As can be seen, the PDF provides at a glance a view of the local atomic correlations in a material.

The PDF analysis process begins with the acquisition of neutron or x-ray total scattering intensity, $S(Q)$, from a powder sample. Q is defined as the momentum transfer of the scattering particle, where $Q = k_{init} - k_{final}$, with k_{init} and k_{final} as the incident and scattered wave-vectors [21]. The experimental atomic pair distribution function, $G(r)$, is generated via the Fourier transform of $S(Q)$ from reciprocal space into real space,

$$G(r) = \frac{2}{\pi}\int_{Q_{min}}^{\infty} Q[S(Q)-1]\sin Qr\,dQ. \tag{3.1}$$

Here, Q_{min} is some small but nonzero minimum measured momentum transfer, which we assume excludes any small-angle scattering resulting from the finite particle size. It is useful to note that Q can be found by $Q = 4\pi\sin\theta/\lambda$, where 2θ is the scattering angle and λ is the wavelength of the incident radiation [21]. $G(r)$ is related to the atomic structure through the relation

$$G(r) = 4\pi r[\rho(r) - \rho_0], \tag{3.2}$$

where ρ_0 is the atomic number density of the material and $\rho(r)$ is the microscopic atomic pair density. The resulting function $G(r)$ yields the probability of finding two atoms separated by the distance r. This overall process is illustrated in Fig. 3.2. In the rightmost panel, the x-axis has real space units of Angstroms. The blue dots are $G(r)$ and the red curve is a fit to the data. The green line found on the bottom of the figure shows the residual between the experimental data and the fit.

Studies of local atomic structure are expected to be valuable for investigations of multiferroics, especially when combined with probes of the local *magnetic* structure. Detailed understanding of short-range atomic and magnetic correlations could potentially provide a direct view into the microscopic mechanisms of magnetoelectric coupling in multiferroics. Several fruitful atomic PDF studies have been conducted on multiferroic systems [27–32], but without corresponding information regarding the local magnetic correlations, resulting in an incomplete picture of the local electronic environment. Magnetic PDF (mPDF) analysis can complete the picture by providing details of local magnetism. Similar to atomic PDF, the mPDF is obtained by Fourier transforming the magnetic total scattering signal, yielding the pairwise magnetic correlations in real space [33,34]. The fundamental quantity defining the mPDF is given by

$$f(r) = \frac{2}{\pi}\int_{0}^{\infty} Q[S_{mag}(Q)-1]\sin Qr\,dQ, \tag{3.3}$$

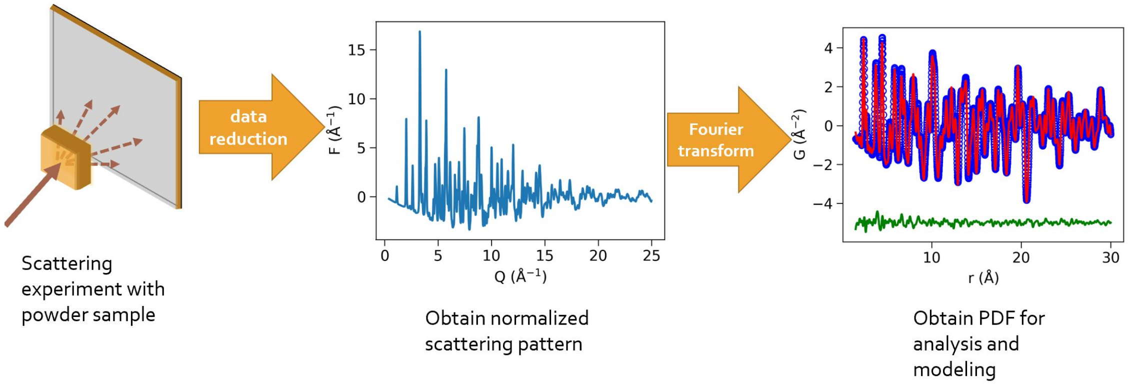

Figure 3.2 Basic procedure for PDF experimentation. Begin by performing x-ray or neutron diffraction experiments with a powdered sample. Next, obtain the resulting reciprocal-space scattering pattern. The PDF is then obtained by applying a Fourier Transform to the data to end up in real space [26]. In the middle figure, F(Å^{-1}) is equivalent to $Q[S(Q)-1]$, the Fourier Transformed term in equation 3.1.

where $S_{mag}(Q)$ is now the magnetic total scattering. Evaluating the Fourier transform yields

$$f(r) = \frac{1}{N}\frac{3}{2(S+1)}\sum_{i\neq j}\frac{A_{ij}}{r}\delta(r-r_{ij}) + B_{ij}\frac{r}{r_{ij}^3}[1-\Theta(r-r_{ij})], \tag{3.4}$$

where the i and j subscripts indicate individual magnetic moments, N represents the number of spins in the systems, S is the spin quantum number in units of $\hbar$, Θ is the Heaviside step function, A_{ij} equals $< S_i^y S_j^y >$, and B_{ij} is $2 < S_i^x S_j^x > - < S_i^y S_j^y >$ [33].

Standard neutron total scattering measurements of magnetic materials produce both the atomic and magnetic PDF together in a single total PDF pattern, allowing for simultaneous investigation of the local atomic and magnetic structures together. For neutron scattering, atomic PDF analysis yields an overall residual between modelled structure behavior and experimental data. Since atomic PDF modelling does not account for magnetic correlations, the residual can be assumed to contain information on the magnetic structure. Thus through a regular PDF fitting, the resulting residual can be used for an mPDF fit, see Fig. 3.3. Initial fits utilize an average structure and then the found fit parameters are then used for the following fits. It is also worth mentioning that PDF has sharper data peaks while mPDF has periodic and broader peaks. This assists in confidently differentiating between the atomic and magnetic signal. Joint atomic and magnetic PDF studies have been successfully conducted for a variety of different magnetic materials [35–42], but this approach has not been applied to multiferroics up to this point.

In spite of similarities in experimentation and data analysis, x-ray and neutron scattering possess many distinct and complementary traits. Performing both types of experiments allows one to check for consistency, yet also access additional information that would not be available if just one experiment type were used. The neutron spin can interact with electronic magnetic moments, making the study of magnetic structure possible [43]. Typically, synchrotron x-ray sources have higher flux than neutron sources. This, combined with the fact that neutron scattering generally has smaller cross-sections, leads to x-ray scattering requiring smaller sample sizes and much faster data collection. X-ray sources typically produce bright, highly collimated beams over a larger energy range, which helps with improved experiment statistics. However, x-rays suffer from the suppression of intensity at high scattering angles due to the atomic form factor, a consequence of the spatial distribution of electron density around the atoms. Because neutrons scatter from the point-like nuclei, they do not have a suppression at larger Q, leading to better statistics at high Q and therefore higher resolution PDF data. The neutron scattering length also varies nonmonotonically with atomic number, while the x-ray scattering strength is proportional to the square of the atomic number. Because of this, it is easier to distinguish neighboring atoms on the periodic table with neutron diffraction. Neutron scattering lengths also vary by isotope, promoting easier differentiation between different isotopes through neutron scattering. Moreover, neutrons more easily scatter lighter elements, causing such elements like hydrogen to be more easily ‘seen’ [44]. Finally, the

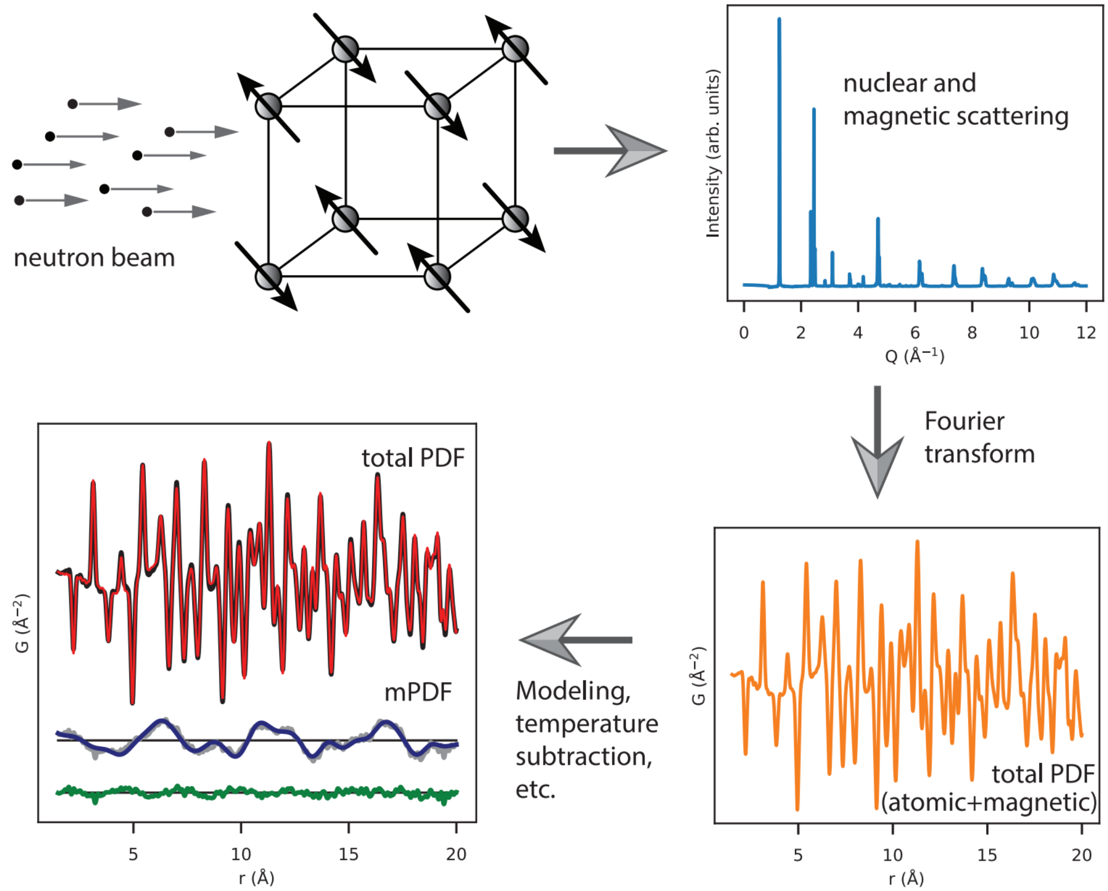

Figure 3.3 Process of obtaining the mPDF fit [45]. Starting with the diffraction pattern obtained from neutron scattering, the diffraction pattern is Fourier transformed to get the total PDF, which includes both the atomic and magnetic PDF signals. After PDF fitting and/or temperature subtraction, the residual of the total atomic PDF contains the magnetic information which can then be fitted to find the magnetic correlations.

energy utilized in neutron scattering does not perturb the targeted atomic system as much, as opposed to high-energy x-ray scattering, where experimental corrections become necessary due to the perturbations.

3.2 Other Techniques Used in this Project

3.2.1 Polarized neutron scattering

Longitudinal ("xyz") polarization analysis of neutron scattering data has been a critical tool in the study of disordered magnetic materials [46]. This process leads to the separation of nuclear, magnetic, and nuclear spin-incoherent contributions of the scattering. Because of this separation of data types, useful magnetic data can be acquired even when the magnetic signal is much smaller than the nuclear signal, such that it could easily be lost or obscured by noise in unpolarized experiments. The separation of these different scattering cross sections is accomplished by the measurement of the spin-flip and non-spin-flip cross sections for various directions of the polarization of the incident neutron beam. More in depth descriptions of the technique can be found elsewhere [46–48].

3.2.2 Muon spin relaxation (μSR)

This technique uses a beam of spin-polarized muons to study the magnetic properties of materials. It is highly sensitive to the presence of static or dynamic magnetism and short-range and long-range correlations alike, although it does not easily yield information about the spatial orientations of magnetic moments [49]. A spin-polarized muon, incident on a sample, will usually stop at an interstitial site of a material, and undergo Larmor procession caused by the local magnetic field (see left hand image of Fig. 3.4). This field is the sum of the internal and externally applied fields. A typical muon lifetime lasts for 2.2 μs, and at this point, the muon experiences an asymmetric decay into a positron, neutrino, and antineutrino particles [50]. The positron, the detected particle, is ejected from the sample preferentially along the direction of the muon spin at the moment of decay [51]. The μSR asymmetry, represented as function of time, $a(t)$, is then recorded as the difference of positron events recorded by two detectors placed on opposite sides (forward and reverse) of the sample. This quantity is proportional to the projection of the net muon spin

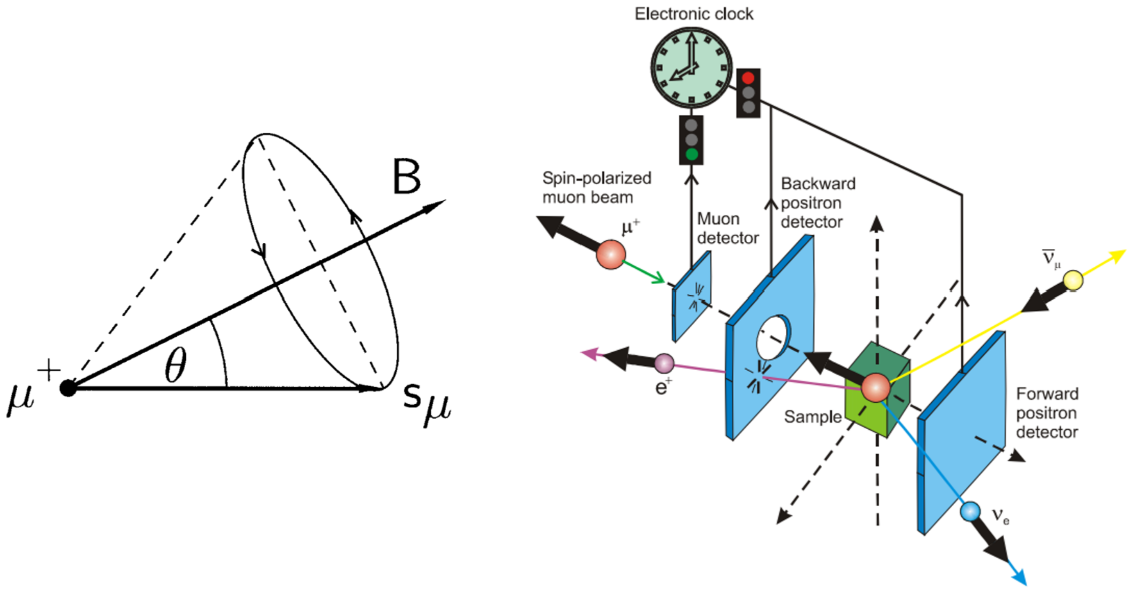

Figure 3.4 The left figure shows Larmor precession of the positive muon (μ^+) with an initial spin-direction (s_μ) in a magnetic field (B). When the muon decays, its decomposition products will be sent in the direction as influenced by the precession. The right figure shows a typical μSr experiment setup, with positron (e^+) detectors in forward and reverse positions in relation to the sample [49, 50]. The muon, along with a positron, will also decay into a neutrino-antineutrino pair (ν_e, $\bar{\nu}_\mu$).

polarization along the direction connecting the two detectors. The behavior of $a(t)$ provides information about the evolution of the local magnetic field distribution across the magnetic phase transition. Importantly, μSR is sensitive both to long- and short-range magnetic correlations, which can be either static or dynamically fluctuating. Fig. 3.4 indicates the basic setup for a zero field (ZF) μSR experiment.

3.3 Experimental Methods

3.3.1 Overview of facilities used

The x-ray diffaction, neutron diffraction, muon spin relaxation, and polarized neutron scattering experiments require specific and highly specialized beamlines at large-scale facilities. We performed x-ray diffraction on beamline 28-ID-1 of the National Synchotron Light SourceII (NSLS-II) at Brookhaven National Laboratory. This beamline is dedicated to atomic PDF and uses a large energy band-pass white x-ray beam from a DW100 damping wiggler source [52]. Neutron diffraction was conducted on the NOMAD instrument of the Spallation Neutron Source at Oak Ridge National Lab. NOMAD is a high-flux, medium-resolution diffractometer that uses a large bandwidth of neutron energies and extensive detector coverage to carry out structural determinations of local order in crystalline and amorphous materials. The enhanced neutron flux, coupled with the advanced neutron optics and detector features, enables high-resolution pair distribution functions [53]. Muon experimentation was performed with the M20D beamline at TRIUMF Laboratory in Vancouver, Canada using the LAMPF spectrometer. This beamline takes muons from the 1AT2 target, typically 10 cm beryllium, and delivers a high flux of surface muons [54]. The LAMPF spectrometer is permanently installed on M20D. Polarized neutron scattering was conducted on the HYSPEC beamline at the Spallation Neutron Source at Oak Ridge National Lab. HYSPEC stands for Hybrid Spectrometer, a unique instrument whose concept combines advantages of the time-of-flight (TOF) technique which traditionally is used at the pulsed sources with those of crystal spectrometers which use continuous neutron beams [55]. A unique feature of HYSPEC is its polarization analysis capability, thereby making it the first polarized beam spectrometer in the SNS instrument suite, and the first successful polarized neutron inelastic instrument at a pulsed spallation source in the world [55]. Photos and diagrams of these beamlines and facilities are shown in Fig. 3.5.

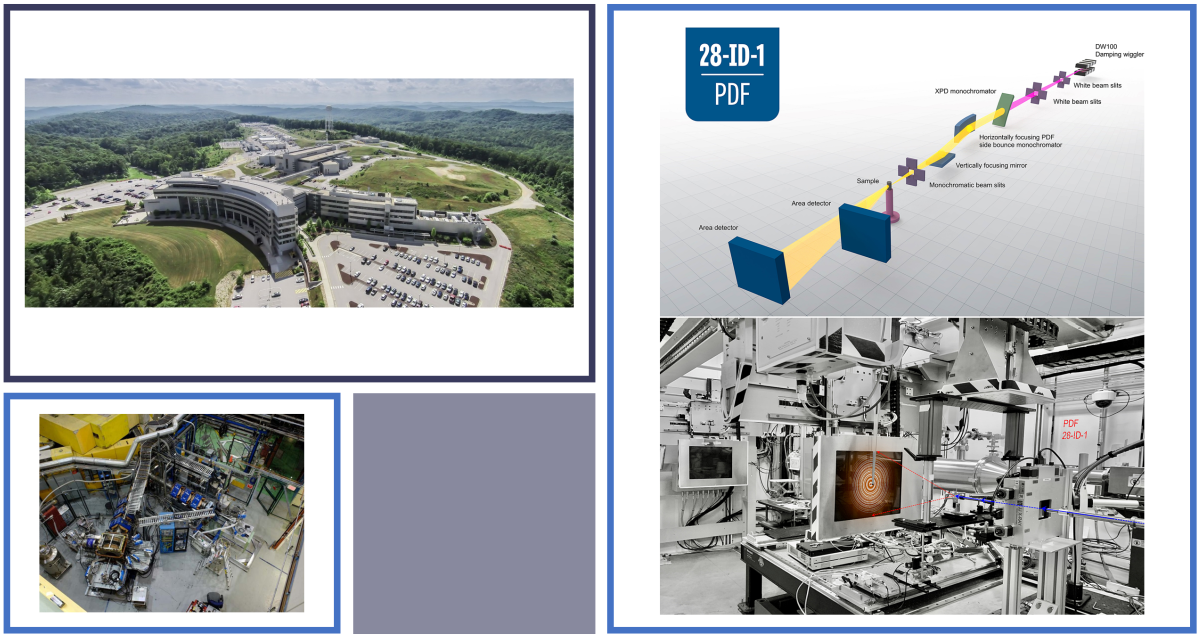

Figure 3.5 Top top right image shows the Spallation Neutron Source at Oak Ridge Labs [56]. The site houses both the NOMAD and HYSPEC beamlines utilized for neutron diffraction studies. The bottom left image contains a visual of the M20D beamline at Triumf on the University of British Colombia campus. On the the right is an image of the beamline structure and beamline room itself of the 28-ID-1 beamline at NSLS-II at Brookhaven Labs.

3.3.2 Sample synthesis and experimental details

Single-phase high-purity polycrystalline powder samples of $Sr_{1-x}Ba_xMn_{1-y}Ti_yO_3$ were synthesized by the group of Omar Chmaissem at Northern Illinois University according to previously published recipes [13, 14]. As $Sr_{1-x}Ba_xMn_{1-y}Ti_yO_3$ pervoskites are metastable, careful material synthesis conditions must be maintained to avoid forming a hexagonal phase. Samples were prepared with stoichiometric mixtures of $SrCO_3$, $BaCO_3$, MnO_2, and TiO_2 in a two step process. The initial step created single-phase, oxygen deficient $Sr_{1-x}Ba_xMn_{1-y}Ti_yO_3$ through solid state ceramic fabrication, with several grinding and heating cycles. Thereafter, the oxygen-deficient samples were annealed in oxygen at 350-450 °C with a slow cooling afterwards to ensure 3.00 ± .01 oxygen atoms per unit formula, confirmed by thermogravimetric analysis. The compositions prepared for the current study were $(x, y) = (0.45, 0), (0.6, 0.05)$, and $(0.7, 0.12)$. The phase purity of each sample was verified through x-ray diffraction. Barium content for the sample of nominal Ba concentration $x = 0.60$ was verified via Rietveld refinement using the program GSAS-II [57]. Fits to x-ray diffraction data utilizing the tetragonal model and Ba concentrations of 0.60 and 0.45 yielded R_w values of 6.596 and 6.815 respectively, as expected based on the nominal composition (see Fig. 3.6).

Further characterization was performed with magnetic susceptibility measurements (M/H) utilizing a Quantum Design Magnetic Property Measurement System (MPMS-3). The data were collected in a field of 1 T upon warming after the samples were cooled to base temperature in zero magnetic field (ZFC-W). We show in Fig. 3.7 the temperature derivative of the magnetic susceptibility for $Sr_{0.55}Ba_{0.45}MnO_3$ and $Sr_{0.4}Ba_{0.6}Mn_{0.95}Ti_{0.05}O_3$. T_N as determined by the maximum of the curve is 193 K for $Sr_{0.55}Ba_{0.45}MnO_3$ and 149 K for $Sr_{0.4}Ba_{0.6}Mn_{0.95}Ti_{0.05}O_3$. These values are consistent with the results published in Ref. [14], confirming the expected magnetic behavior for these samples. We note that the ferroelectric behavior of samples of similar composition prepared by identical methods was confirmed in Ref. [12]. For the purposes of the current study, verifying the expected systematic behavior with Ba concentration is far more important than knowing the exact composition with high precision.

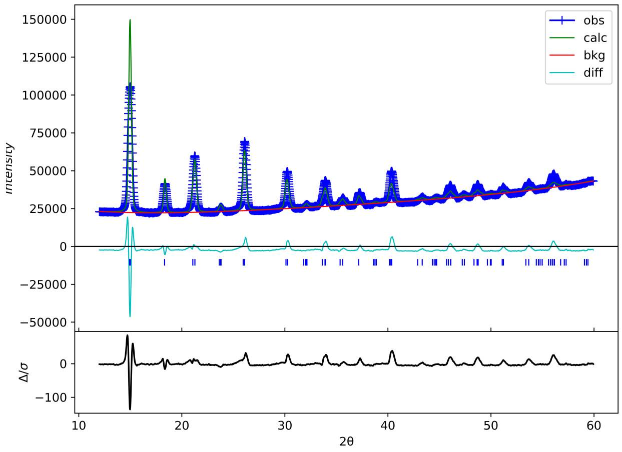

Figure 3.6 Rietveld refinement through the program GSAS-II of $Sr_{0.4}Ba_{0.6}Mn_{0.95}Ti_{0.05}O_3$ using the nominal composition with $x = 0.60$. Compared to refinements with $x = 0.45$, the nominal composition produces the best fit.

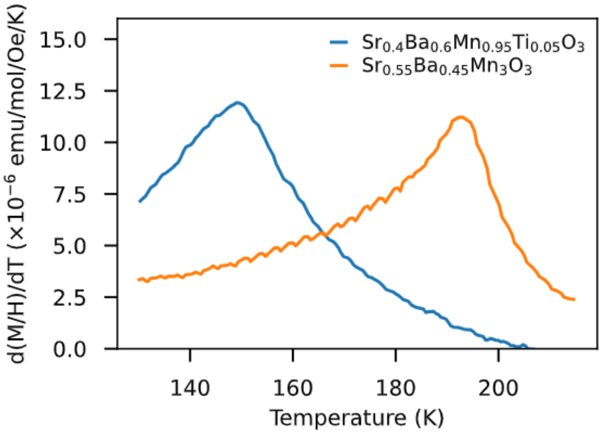

Figure 3.7 Temperature derivative of the magnetic susceptibility of $Sr_{0.4}Ba_{0.6}Mn_{0.95}Ti_{0.05}O_3$ and $Sr_{0.55}Ba_{0.45}MnO_3$ as a function of temperature. Maxima occur at 149 K and 193 K, respectively. The measurements were taken in a field of 1 T using a zero-field-cooling protocol.

For the neutron total scattering experiments, samples of mass $\sim$200 mg were loaded into thin quartz capillaries and mounted on the NOMAD beamline. Diffraction patterns with a total integrated proton charge of 4 C were collected at a series of temperatures between 90 and 500 K using a nitrogen cryostream to control the temperature. The time-of-flight scattering data were reduced and Fourier transformed with $Q_{\mathrm{max}} = 30$ Å^{-1} to produce the PDF data using the ADDIE software [58]. For the x-ray total scattering measurements performed on beamline 28-ID-1 at NSLS-II, samples of mass $\sim$15 mg were loaded into polyimide capillaries placed in a liquid helium cryostat, and mounted on the beamline. We collected scattering patterns between 5 K and 500 K in steps of 5 K. The resulting diffraction patterns were azimuthally integrated using pyFAI [59] and normalized and Fourier transformed into the PDF data using xPDFsuite [60]. Models of the atomic structure were fit to the neutron and x-ray PDF data using PDFgui [61]. Magnetic PDF fits were carried out using the `diffpy.mpdf` package [62]. We note that the total scattering data recorded in both the neutron and x-ray experiments contain scattering intensity integrated over all energy transfers, and the PDF therefore corresponds to the instantaneous local structure of the material.

For the polarized neutron scattering measurements performed on HYSPEC, the energy of the incident neutrons was $E_i = 28$ meV, and the frequency of the Fermi chopper was 60 Hz. The data were integrated over energy transfers from -3 to 3 meV. Spin-flip (SF) and non-spin-flip (NSF) data were collected with the neutron polarization oriented parallel to the Q vector corresponding to the elastic scattering at the center of the 60° detector bank, for six different detector positions. The total 2θ scattering range covered by the measurements was 4 - 111°. The flipping ratio was found to be 14 through measurements of the nuclear Bragg peaks in both the SF and NSF channels. MANTID was used to implement post-processing data corrections for the angle-dependent supermirror transmission and flipping ratio efficiency [55, 63]. In this study, the magnetic scattering is determined as the intensity measured in the SF channel corrected for the flipping ratio using Eq. 2 in Ref. [55].

The powder samples were pressed into pellets for the μSR experiments. The pellets were mounted on a low-background sample holder using aluminized mylar tape. The temperature was controlled with a liquid helium cryostat. We performed the μSR data analysis using the open source program BEAMS [64].

Chapter 4

Results

4.1 Characterization of the local atomic structure

We first present results relating to the local atomic structure of (Sr,Ba)(Mn,Ti)O_3 determined from atomic PDF analysis of the neutron and x-ray total scattering data. We begin with model-independent analysis of the data, which we then support through quantitative refinements of structural models.

4.1.1 Model-independent analysis

To illustrate the temperature dependence of the structure on a qualitative basis, we display in Fig. 4.1 the PDF data for $Sr_{0.55}Ba_{0.45}MnO_3$ at various temperatures across the ferroelectric transition ($T_C =$ 350 K). Two data ranges are shown: 1.5 – 10 Å, revealing the local structure, and 40 — 50 Å, corresponding to intermediate-range structural correlations. The PDF patterns remain nearly unchanged with temperature over the shorter range, with only a slight broadening and shifting of the peaks to higher r visible as the temperature is raised from 255 K to 490 K. No abrupt change occurs across T_C (highlighted by the red PDF curve). In contrast, clear and abrupt changes are seen across T_C when inspecting the PDF patterns over the longer data range, such as a rightward shift of the

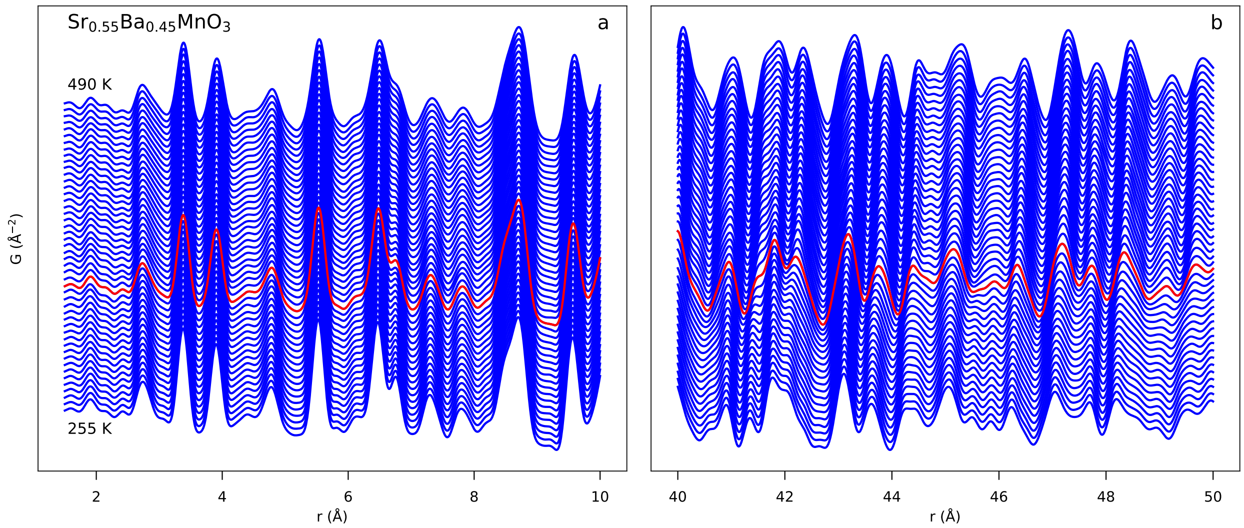

Figure 4.1 X-ray PDF data for $Sr_{0.55}Ba_{0.45}MnO_3$ between 250 K and 490 K displayed over the range 1.5 – 10 Å (a) and 40 – 50 Å (b). The PDF patterns were collected in increments of 5 K and are offset vertically on the plot for clarity. For the viewing range at higher r, clear and abrupt changes are evident across the ferroelectric transition at 350 K (red PDF pattern). No abrupt changes are observed in the low-r viewing range. Figure produced by Dr. Frandsen.

shoulder peak centered around 42 Å, a merging of the small peaks between 45.5 Å and 46 Å, and many other systematic changes as the temperature increases across T_C. Thus, the structural change corresponding to the ferroelectric transition at T_C is clearly evident in the data over sufficiently long length scales such as 40 – 50 Å, while the local structure shows no such change. We can therefore infer that the instantaneous local structure is already symmetry-broken well above T_C due to short-range ferroelectric distortions.

To investigate this further, we computed the Pearson correlation coefficient between each PDF pattern and the patterns collected at every other temperature for a given sample. This quantity, given by

$$R = \frac{\sum_i (G_{1,i} - \langle G_1 \rangle)(G_{2,i} - \langle G_2 \rangle)}{\sqrt{\sum_i (G_{1,i} - \langle G_1 \rangle)^2 \sum_i (G_{2,i} - \langle G_2 \rangle)^2}} \tag{4.1}$$

can be used as a measure of the similarity between two data sets G_1 and G_2, with angular brackets denoting the mean. The Pearson coefficient ranges from 1 to -1, with 1 indicating perfect linear correlation, 0 indicating no correlation, and -1 indicating anti-correlation between the two data sets. We computed the coefficient for the data ranges 1.5 – 21.5 Å and 41.5 – 61.5 Å to allow a comparison of the local and longer-range structure once again. The resulting Pearson correlation maps are shown for $Sr_{0.55}Ba_{0.45}MnO_3$ in Fig. 4.2 using both neutron and x-ray PDF data. These plots can be read by selecting a pair of temperatures whose data sets are to be compared, locating the intersection of these two temperature points on the plot, and then comparing the observed color at that point to the color bar shown to the right of each plot. The main diagonal from lower left to upper right always has a coefficient of unity (since the diagonal corresponds to each data set being compared to itself), and the maps are symmetrical when reflected across the main diagonal. Bright colors indicate a high level of similarity between PDF data collected at the corresponding temperatures, while dark colors indicate less similarity. Panels (a) and (c) in Fig. 4.2 show the correlations calculated from the neutron PDF data, which were collected at 10 temperatures between 90 and 500 K indicated by the dashed gray lines. Panels (b) and (c) show the corresponding x-ray PDF results using data collected in steps of 5 K between 5 and 500 K. The top and bottom panels show the correlation coefficients calculated from the shorter and longer data ranges, respectively.

Several features of the correlation plots bear mentioning. As can be seen by the color scales, the overall variation across the full temperature range is significantly less for the shorter data range than for the longer data range, consistent with our inspection of the PDF data in Fig. 4.1. The ferroelectric and antiferromagnetic transitions are identifiable in the longer data range as relatively sharp changes in the correlation coefficient in certain regions of the correlation maps. Specifically, a rapid variation is visible in the long-range x-ray data Fig. 4.2(d) when traversing 350 K, corresponding to the expected T_C of this composition. This indicates that the structure on the length scale of 41.5 – 61.5 Å changes significantly and abruptly across 350 K.

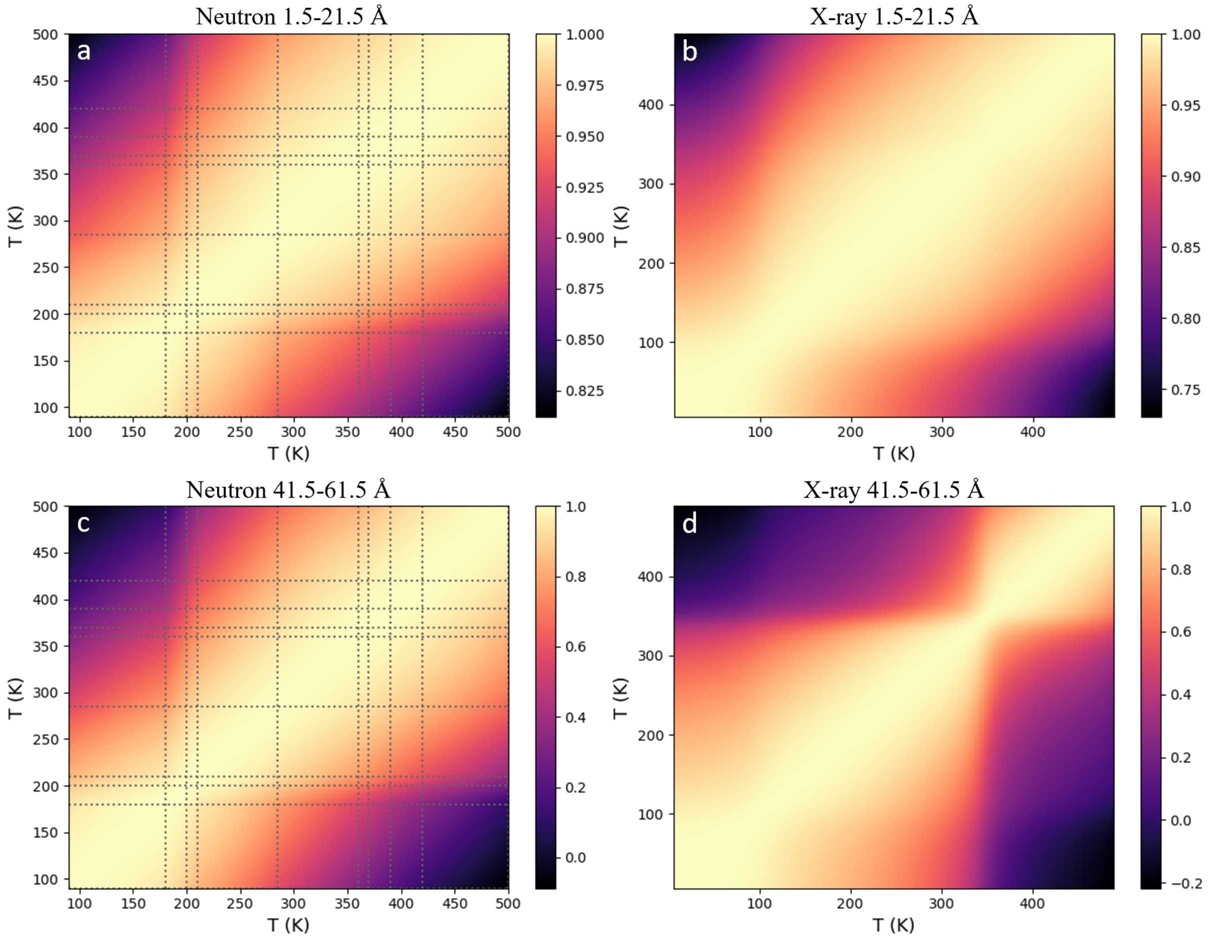

Figure 4.2 Color maps of the Pearson correlation coefficient for pairs of PDF data sets obtained from $Sr_{0.55}Ba_{0.45}MnO_3$ at various temperatures. (a, b) Correlation coefficients computed for PDF data in the range 1.5 – 21.5 Å using neutrons and x-rays, respectively. (c, d) Same as (a, b), except that the data range 41.5 – 61.5 Å was used. Vertical and horizontal dashed lines in (a) and (c) mark the temperatures at which neutron PDF data were collected. X-ray data were collected on a uniform temperature grid between 5 K and 500 K in steps of 5 K.

In contrast, the variation across 350 K for the short-range data Fig. 4.2(b) is much less pronounced, again supporting the idea that the local structure is already symmetry-broken above T_C and does not undergo any significant rearrangement at the long-range ferroelectric transition. Evidence of a structural change is less visible for the long-range neutron data Fig. 4.2(c), which we attribute primarily to sparser temperature coverage across T_C compared to the x-ray data. On the other hand, the antiferromagnetic transition can be seen in both the short- and long-range neutron data Fig. 4.2(a, c) around 200 K, the expected T_N for this composition. The x-ray results also show a variation in the correlation coefficients across $\sim$120 K, albeit much less well-defined than the transition visible at 350 K. We attribute this feature at 120 K to the antiferromagnetic transition. The discrepancy with the expected Néel temperature of 200 K is due to known issues with low-temperature equilibration for insulating samples in the cryostat used on the x-ray PDF beamline; in other words, although the nominal cryostat temperature may be 120 K, the actual sample temperature could be much higher, such as 200 K.

Some caution must be exercised when basing a claim of local symmetry breaking (such as the one we made in the previous discussion) on the observation that the low-r region of the PDF shows a higher Pearson correlation as a function of temperature than high-r regions. The magnitude of the shifts in PDF peak positions due to thermal expansion scales proportionally with r. Therefore, even for a conventional material in which the local structure shows no deviations from the average structure, correlation maps such as the ones displayed in Fig. 4.2 will always show higher correlations for shorter data ranges than for longer data ranges. To verify that the correlation maps generated from our PDF data actually contain evidence for local symmetry breaking rather than merely thermal expansion, we corrected the computed Pearson correlations for the effects of thermal expansion as follows.

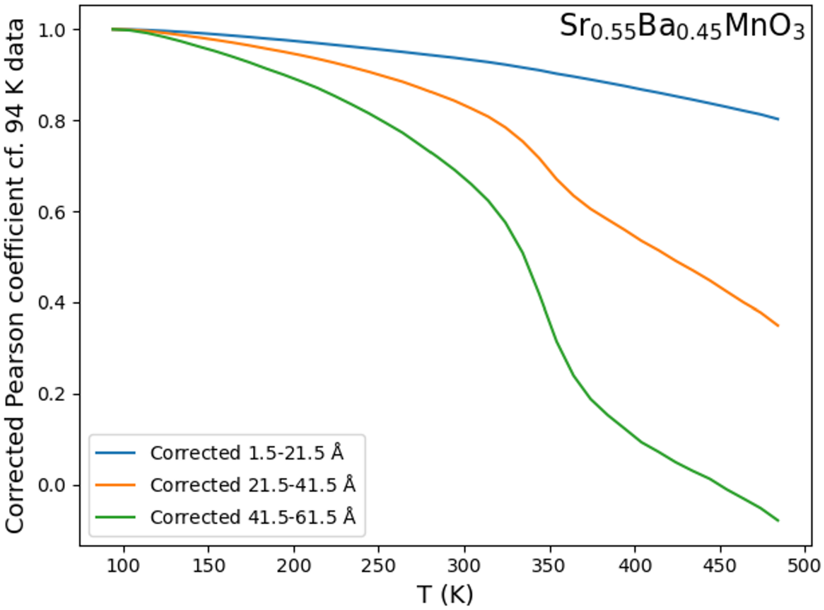

Figure 4.3 Pearson correlation coefficient for $Sr_{0.55}Ba_{0.45}MnO_3$ with respect to the x-ray PDF data collected at 90 K, corrected for thermal expansion as explained in the main text. Three different data ranges are used. The ferroelectric transition around 350 K is most evident for the highest r-range but essentially invisible for the shortest data range, confirming that the local structure is already symmetry broken above T_C.

First, we performed fits in PDFgui to representative low-temperature (90 K), intermediate-temperature (285 K), and high-temperature (500 K) data sets. We then simulated the PDF pattern at 90 K and 500 K using the lattice parameters refined at those specific temperatures but all other structural parameters (atomic coordinates, atomic displacement parameters, and the linear sharpening parameter in PDFgui) as determined by the refinement at the intermediate temperature. Thus, the differences between the two calculated PDFs are due solely to the thermal shifts of the lattice parameters. The Pearson correlation coefficient between these two simulated PDF patterns was then calculated over the desired data range. We will call this coefficient R_{th}. The quantity $\Delta R_{th} = 1 - R_{th}$ then represents the contribution of thermal expansion to the differences between the data sets collected at 90 and 500 K. By adding ΔR_{th} to the experimental Pearson correlation coefficient R_{exp} computed from the actual data sets, we obtain a corrected correlation coefficient $R_{\mathrm{c}} = R_{\mathrm{exp}} + \Delta R_{\mathrm{th}}$ for which the influence of thermal expansion has been removed (albeit crudely). To apply this correction to the correlation coefficients calculated for all other temperatures with respect to 90 K, the correction term ΔR_{th} was scaled linearly from 0 at 90 K to its maximum value at 500 K, which presupposes linear thermal expansion.

The temperature dependence of the corrected Pearson correlation coefficient with respect to the 90 K x-ray PDF data for $\mathrm{Sr_{0.55}Ba_{0.45}MnO_3}$ is displayed for three different data ranges in Fig. 4.3.

As the temperature increases toward and across T_{C}, the shorter data ranges show higher correlation coefficients (both corrected and uncorrected) than the long data range. This further supports the idea that the local structure undergoes no sharp change across T_{C} because the local symmetry is already broken in the paraelectric state. The transition appears as step-like change around 350 K in the correlation curve for the 41.5 – 61.5 Å data range, with a slightly broader step observed for 21.5 –41.5 Å. Similar results are found for the neutron PDF data and for the other compositions.

4.1.2 PDF boxcar fits

Complementing the model-independent analysis presented in the previous section, we now present structural refinements of the tetragonal model against the PDF data. We used a boxcar fitting approach, in which the structural model was refined against a sliding window through the PDF data. In our case, we performed fits over a 20 Å range beginning with 1.5 – 21.5 Å and ending with 41.5 –61.5 Å in increments of 2 Å, resulting in 21 distinct fitting ranges for each temperature and hundreds (for the neutron data) or thousands (for the x-ray data) of fits for each sample studied. This enables a very detailed study of the evolution of the local structure (as determined from the shorter range fits) to the intermediate or average structure (as determined from the longer range fits). We used the tetragonal model at all temperatures, including those in the nominally cubic phase, to

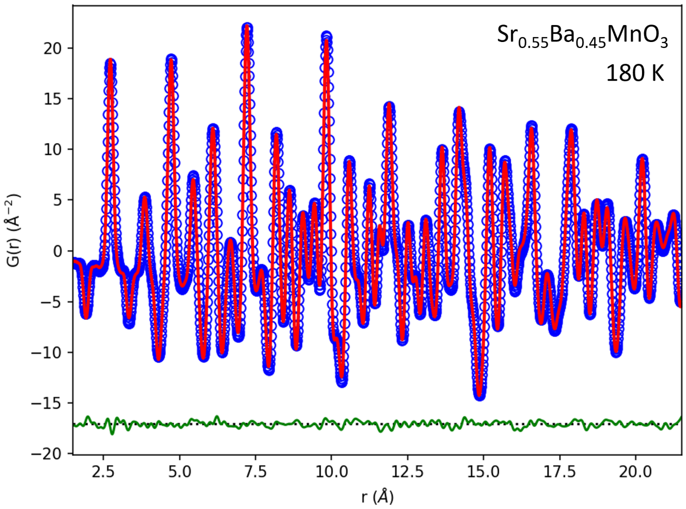

Figure 4.4 Representative neutron PDF fit for $Sr_{0.55}Ba_{0.45}MnO_3$ at 180 K. The blue symbols show the experimental data, the red curve the best fit, and the green curve the fit residual, offset vertically for clarity.

avoid imposing the symmetry of the average structure on the local structure. In the case that the structure really is cubic, the tetragonal lattice parameters will simply converge to equal values in the fit.

The structural parameters refined in PDFgui included a scale factor, the lattice parameters, the coordinates of the atoms with symmetry-allowed positional degrees of freedom, the ADPs, and the linear correlated motion sharpening parameter for the fits that included data below 5 Å. The z coordinates of the atoms on the Mn site were fixed so that the positions of the other atoms could shift relative to the Mn sites. The goodness-of-fit metric R_w typically lay between 0.05 to 0.10, indicating good quality fits. A representative fit is shown in Fig. 4.4, obtained from neutron PDF data for $Sr_{0.55}Ba_{0.45}MnO_3$ at 180 K.

The refined lattice parameters were extracted from each fit conducted for a given sample. This allows us to quantify the temperature- and length-dependent behavior of the tetragonal (i.e. ferroelectric) distortion by calculating c/a for every fit. The results for $\mathrm{Sr_{0.55}Ba_{0.45}MnO_3}$ based on neutron PDF fits are shown in Fig. 4.5(a). The globally ferroelectric phase is seen as the bright, horizontal band beginning at 350 K and extending to 200 K, below which AFM order sets in. We see that the the tetragonal distortion persists for all fitting ranges (albeit with a diminished magnitude) in the AFM phase, thereby confirming the multiferroic nature of the system. The reduced tetragonal distortion in the multiferroic phase is consistent with previous reports [8, 13]. At temperatures above 350 K, the long-range fits converge to $c/a = 1$, evident as the dark region in the upper right corner of the plot. This is consistent with global cubic symmetry in the paralectric state. In contrast, the short-range fits with $r_{\mathrm{mid}} \lesssim 20$ Å reveal a clear local tetragonal distortion that diminishes with increasing distance. Vertical cuts along $r_{\mathrm{mid}} = 15.5$ Å and 28.5 Å are shown in Fig. 4.5(b), further illustrating the difference between the shorter- and longer-range fits. This directly validates the previous conclusion based on our model-independent analysis that the instantaneous local structure is already symmetry-broken above the ferroelectric Curie temperature. Interestingly, a local enhancement of the tetragonal distortion also seems to be present in the multiferroic state at low temperature.

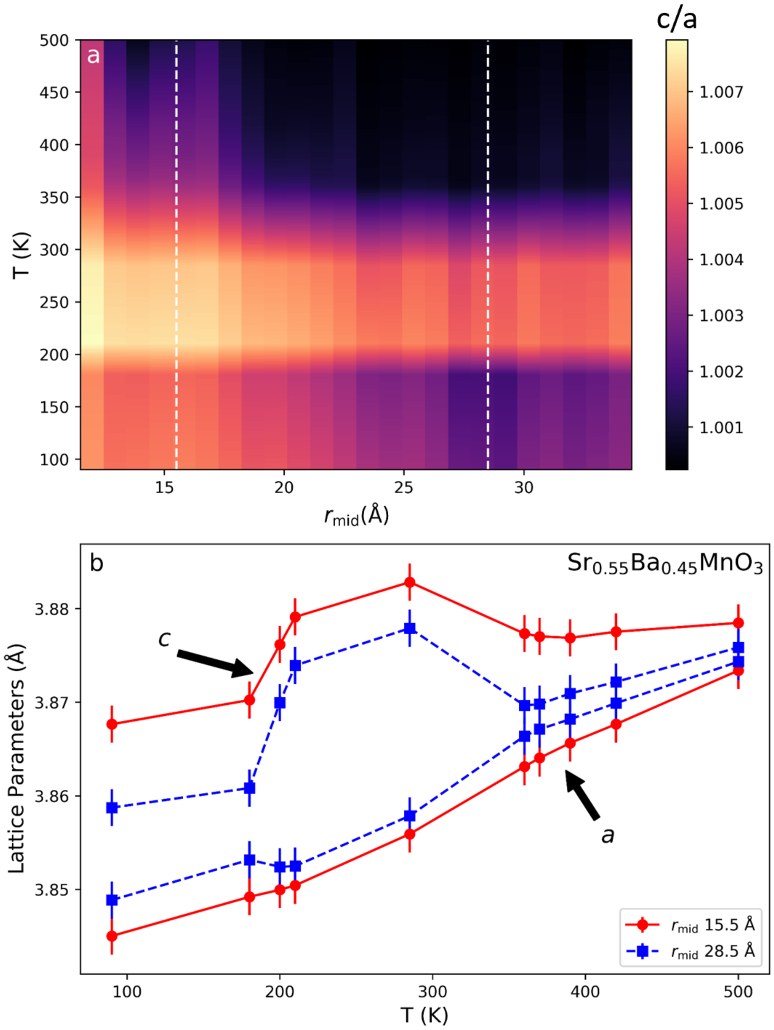

Figure 4.5 (a) Tetragonal distortion c/a in $Sr_{0.55}Ba_{0.45}MnO_3$ as a function of temperature and fitting range, as determined by PDF boxcar fits to the neutron PDF data. The horizontal axis indicates the midpoint of the 20-Å fitting range r_{mid}. Brighter (darker) colors correspond to a greater (lesser) tetragonal distortion. Linear interpolation was used between discrete (r_{mid}, T) points. (b) Lattice parameters extracted from the fits with $r_{\mathrm{mid}} = 15.5$ Å and 28.5 Å, corresponding to the vertical dashed lines in (a).

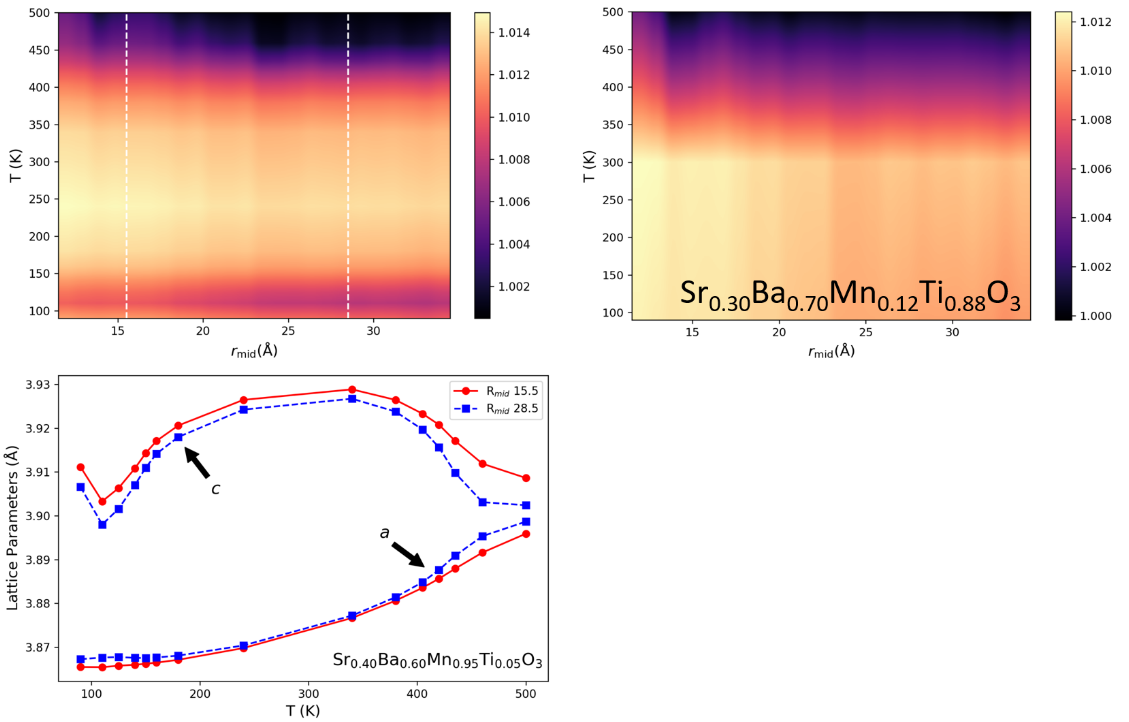

Figure 4.6 Color maps encapsulating the same basic pattern as a function of temperature and r-range as seen in Fig. 4.5. The plot on the right for $Sr_{0.3}Ba_{0.7}Mn_{0.88}Ti_{0.12}O_3$ only has data taken at 90 K, 300 K, and 500 K, so no cuts along specific r ranges were taken.

Additional results for neutron scattering from different compositions of (Sr,Ba)(Mn,Ti)O_3 are shown in Fig. 4.6. These other compositions show similar, but not as prominent, behavior as a function of temperature and r-range in comparison with $Sr_{0.55}Ba_{0.45}MnO_3$. Scattering experiments were performed at only three temperatures for $Sr_{0.3}Ba_{0.7}Mn_{0.88}Ti_{0.12}O_3$, making it more difficult to identify the trends reliably. X-ray data is shown in Fig. 4.7, which also shows a similar pattern. The x-ray fits were unstable in some regions, resulting in a rapidly varying c/a ratio in the corresponding areas of the plots in Fig. 4.7. Instabilities in x-ray fits were most likely caused by the reduced signal strength of the x-ray PDF data at high r. The x-ray diffraction patterns used to generate the PDF have relatively low resolution in reciprocal space, leading to faster damping in real space compared to neutron PDF data.

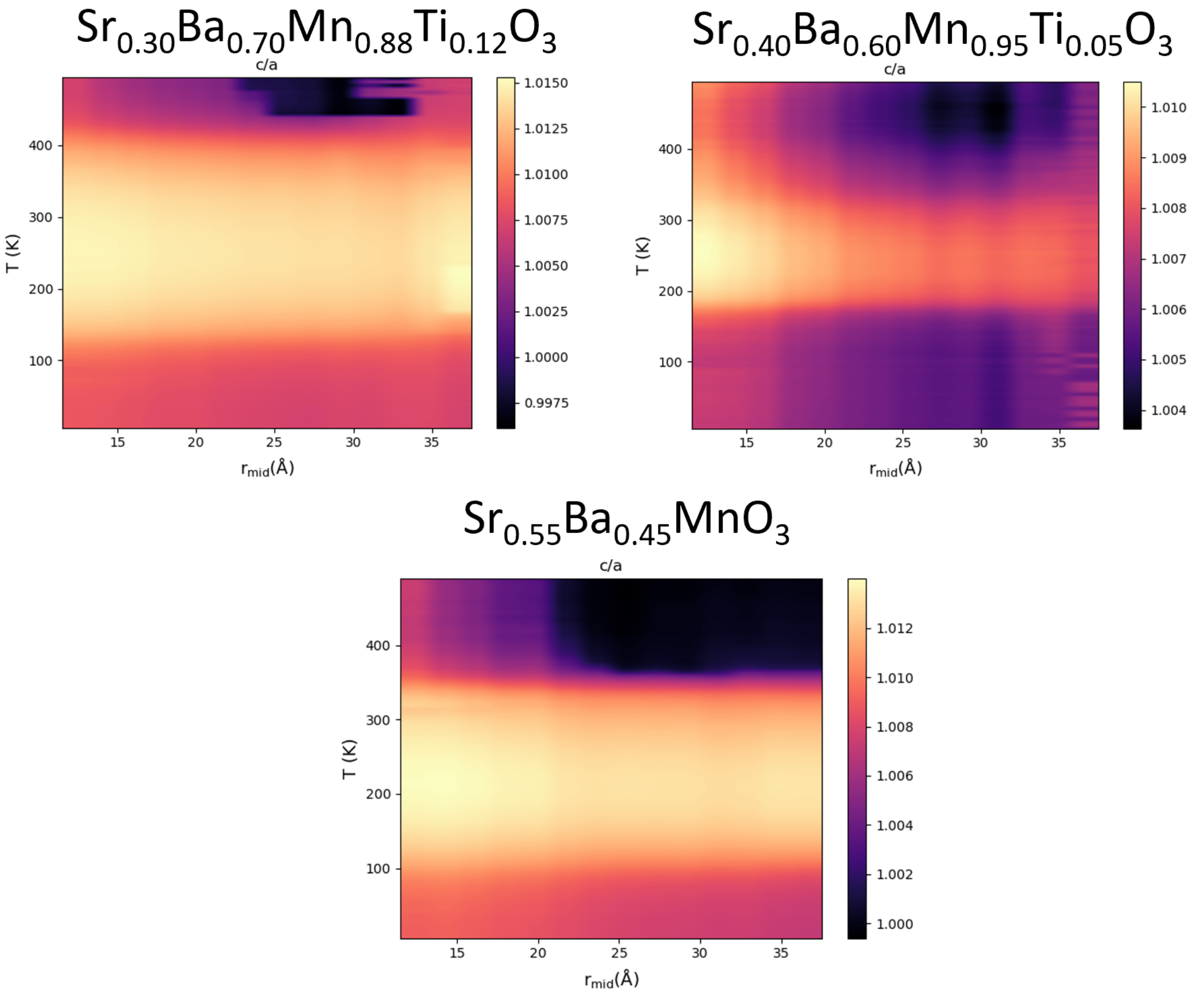

$Sr_{0.30}Ba_{0.70}Mn_{0.88}Ti_{0.12}O_3$

$Sr_{0.40}Ba_{0.60}Mn_{0.95}Ti_{0.05}O_3$

$Sr_{0.55}Ba_{0.45}MnO_3$

Figure 4.7 Color map of the lattice distortion as determined through x-ray PDF. Similar patterns exist in comparison with Fig. 4.5, which utilizes neutron diffraction data, but some discrepancies exists because of instabilities in the x-ray fits, particularly at high *r*. Notice that for certain plots the minimum value dips below 1.0, such that the *a*-lattice is *slightly* larger than the *c*-lattice.

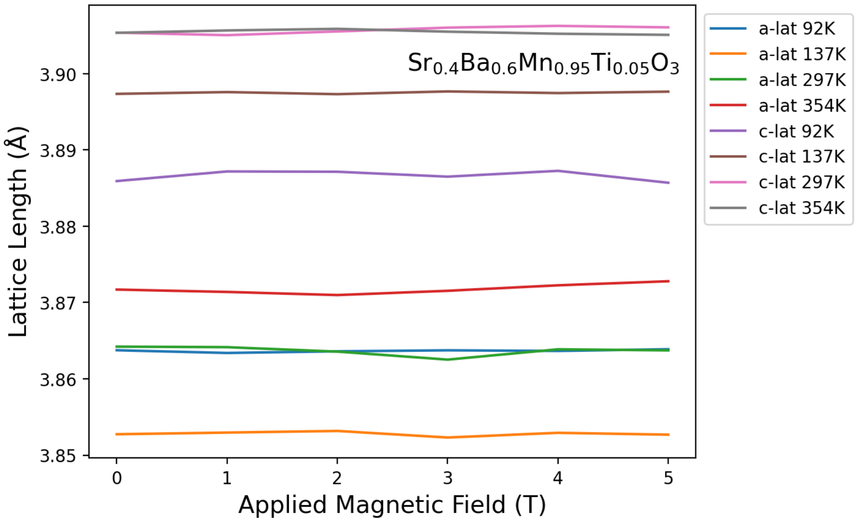

Figure 4.8 There is no direct relationship appearing between lattice structure and applied magnetic field. Xray data was taken at four temperatures for $Sr_{0.4}Ba_{0.6}Mn_{0.95}Ti_{0.05}O_3$.

As a final note on the structural characterization of $(Sr,Ba)MnO_3$, we also comment on x-ray PDF measurements that we performed with variable temperature in an *in situ* magnetic field up to 5 T. No clear field dependence of any structural parameters at any temperature could be determined from the fits, as seen in Fig. 4.8, indicating that if such effects are present, they are smaller than the sensitivity of our x-ray PDF measurements. This is not a surprising result, considering that antiferromagnets do not typically show a large response to an applied magnetic field.

4.2 Characterization of the local magnetic structure

We now present data relating to the local magnetic structure of (Sr,Ba)(Mn,Ti)O_3, with particular emphasis on short-range magnetic correlations above T_N. We begin with magnetic PDF analysis, followed by polarized neutron scattering, and finally μSR.

4.2.1 Magnetic PDF analysis

Magnetic PDF data are typically extracted from the total PDF (i.e. the sum of the nuclear and magnetic PDF signals) by subtracting the best-fit nuclear PDF from the total PDF data. The resulting fit residual contains the mPDF signal in addition to the usual components of the fit residual, e.g. statistical noise (very small given the counting statistics used for the data collection), systematic errors such as imperfect background subtraction, and possibly errors from the nuclear PDF fit. In (Sr,Ba)(Mn,Ti)O_3, the mPDF is quite small in magnitude, comparable to the systematic errors. Therefore, we took the additional step of subtracting the nuclear PDF fit residual obtained at a high temperature ($\gtrsim$ 350 K, high enough that no short-range magnetic correlations survive) from the fit residuals at all lower temperatures. This removes the temperature-independent systematic errors caused by the imperfect background subtraction, which would otherwise swamp the mPDF signal.

In Fig. 4.9(a), we plot the total neutron PDF fit for $Sr_{0.4}Ba_{0.6}Mn_{0.95}Ti_{0.05}O_3$ at 100 K (top set of red and blue curves), together with the isolated mPDF signal and fit (middle set of gray and blue curves). This demonstrates the small signal weight of the mPDF relative to the total PDF. We show a close-up view of the mPDF data and fit in Fig. 4.9(b). The fit agrees well with the data, confirming that we are sensitive to the magnetic signal in the data. The mPDF signal is characteristically broader and lower in frequency than the nuclear PDF, so there is minimal risk of inadvertently fitting the mPDF model to deficiencies in the nuclear PDF model.

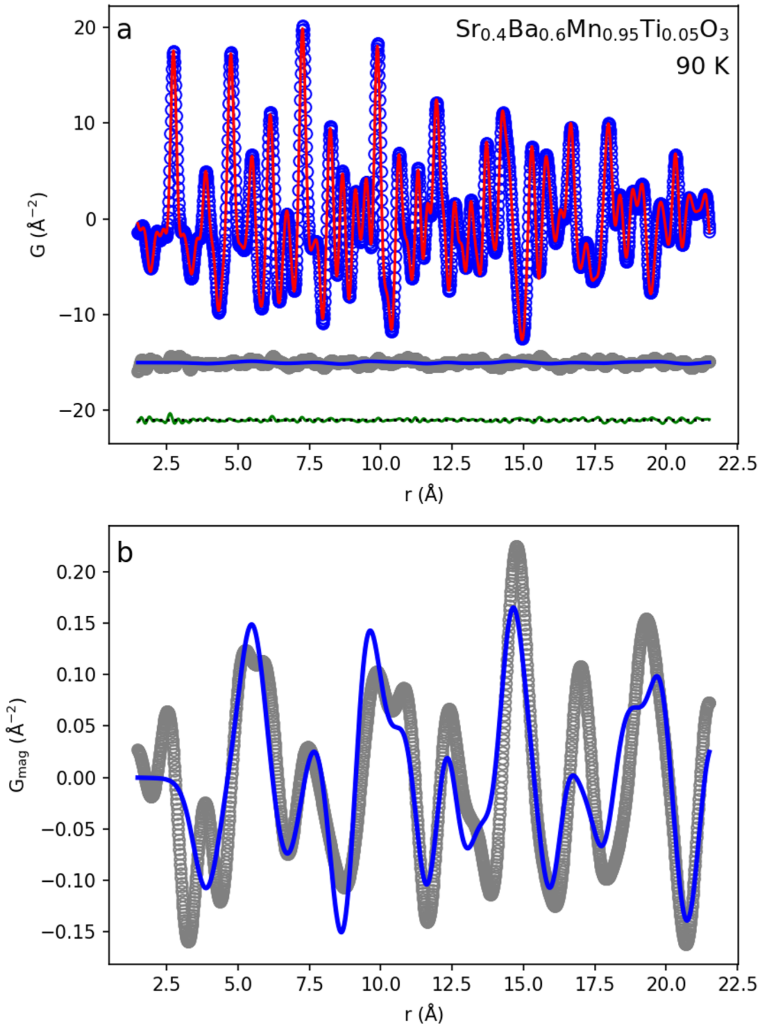

Figure 4.9 (a) Neutron PDF fit to $Sr_{0.4}Ba_{0.6}Mn_{0.95}Ti_{0.05}O_3$ at 100 K. The top set of curves shows the data (blue symbols) and total PDF fit (red curve). The gray curve offset vertically below is the isolated mPDF signal, i.e. the total experimental PDF signal with the calculated nuclear PDF and the nuclear PDF fit residual from 340 K subtracted. The best-fit mPDF based on the known G-type AFM order is overlaid in blue. The overall fit residual is shown in green at the bottom of the figure. (b) Zoomed-in view of the mPDF signal (gray curve) and fit (blue curve). The experimental signal has been smoothed via a Fourier filter that removes contributions beyond 6 Å^{-1}, where the magnetic scattering intensity is negligible due to the magnetic form factor.

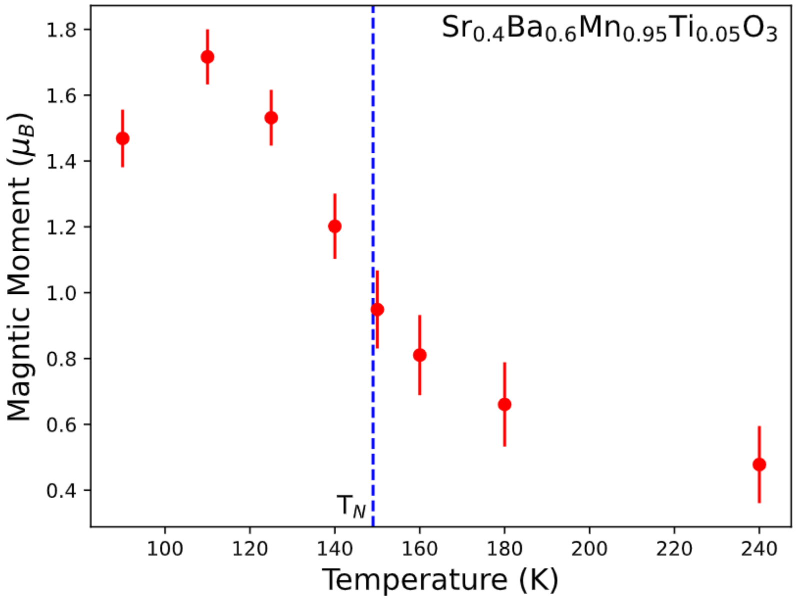

Figure 4.10 Locally ordered magnetic moment in $Sr_{0.4}Ba_{0.6}Mn_{0.95}Ti_{0.05}O_3$ obtained from mPDF analysis. The persistent ordered moment above T_N arises from short-range AFM correlations. The anomalous drop in the ordered moment at 90 K is expected to be an artifact of imperfect thermal equilibrium.

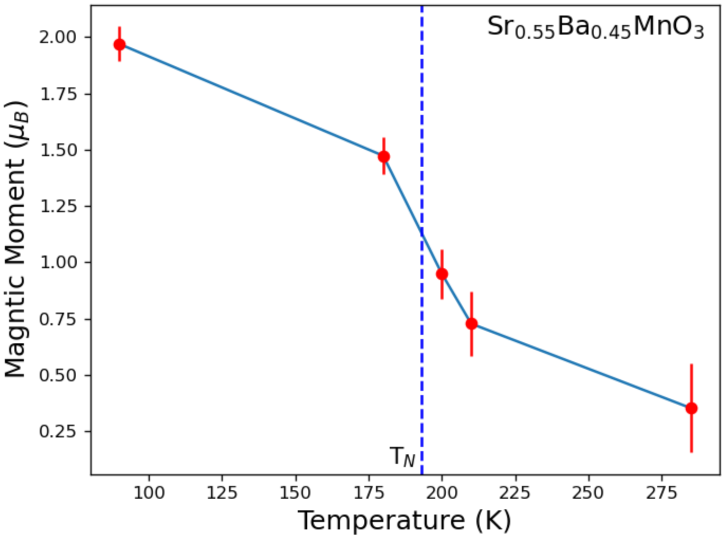

Figure 4.11 Locally ordered magnetic moment in $Sr_{0.55}Ba_{0.45}MnO_3$ obtained in the same process as $Sr_{0.4}Ba_{0.6}Mn_{0.95}Ti_{0.05}O_3$ in Fig. 4.10. Data was collected at fewer temperatures, but the same behavior persists, as LMOP decreases as temperature increases but remains nonzero above T_N. For this material, $T_\text{N} \approx 193$ K.

We performed mPDF fits to the neutron PDF data for $Sr_{0.55}Ba_{0.45}MnO_3$ and $Sr_{0.4}Ba_{0.6}Mn_{0.95}Ti_{0.05}O_3$ for all temperatures below 350 K, from which we extracted the local magnetic order parameter (LMOP) as a function of temperature. This should be interpreted as the magnitude of the instantaneous locally ordered moment among near-neighbor Mn^{4+} spins, which will remain nonzero even above T_N when short-range magnetic correlations are present. We plot the LMOP for $Sr_{0.4}Ba_{0.6}Mn_{0.95}Ti_{0.05}O_3$ and $Sr_{0.55}Ba_{0.45}MnO_3$ in Fig. 4.10 and Fig. 4.11 respectively.

The ordered moment decreases gradually with temperature, as expected, but clearly remains nonzero up to at least 240 K, which is 100 K above the long-range AFM transition temperature $T_N = 149$ K (blue vertical line). Similar results are seen for $Sr_{0.55}Ba_{0.45}MnO_3$. This provides direct and quantitative evidence for short-range magnetic correlations above T_N in (Sr,Ba)MnO_3.

4.2.2 Polarized neutron scattering

Considering the small magnitude of the mPDF signal relative to the total PDF, it is useful to confirm the presence of short-range magnetic correlations above T_N using polarized neutron scattering, which provides excellent sensitivity to diffuse magnetic scattering. In Fig. 4.12, we plot the spin-flip (magnetic) scattering cross section of $Sr_{0.4}Ba_{0.6}Mn_{0.95}Ti_{0.05}O_3$ at 100 K (below T_N) in panel (a) and 160 K (above T_N) in panel (b). The experimental data, shown by the black symbols, exhibit sharp magnetic Bragg peaks below T_N and diffuse peaks above T_N, indicative of long-range and short-range magnetic correlations, respectively. The red curves are the calculated scattering patterns using a model of the G-type AFM order consisting of long-range and short-range correlations, respectively, showing reasonable agreement with the data. The magnetic peaks at 100 K are indexed by the propagation vector $k = (1/2, 1/2, 1/2)$ and were modeled using the magnetic space group I_c4cm in BNS notation and $I4cm.1'_c[rP4mm]$ in the new unified (UNI) notation [65] with corresponding lattice transformation $(a-b, a+b, 2c)$. The Mn moment is parallel to the c-axis and was refined to be 1.49(1) μ_B at 100 K. Quantitative agreement between the data and model

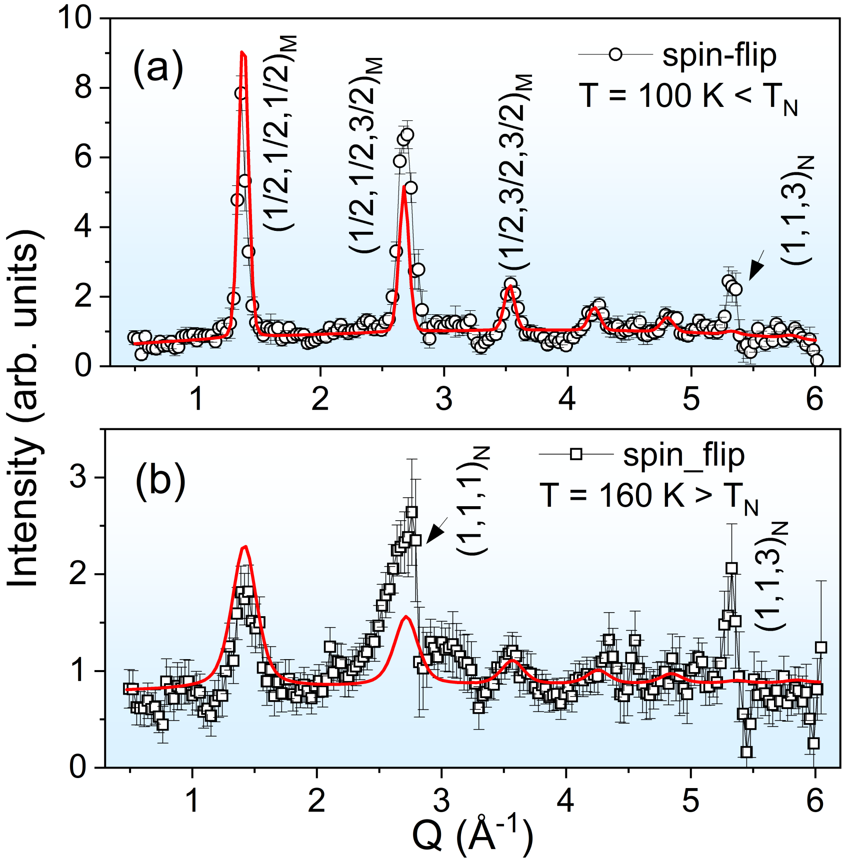

Figure 4.12 Spin-flip magnetic scattering from $Sr_{0.4}Ba_{0.6}Mn_{0.95}Ti_{0.05}O_3$ at 100 K [(a); AFM state] and 160 K [(b); PM state]. The black symbols show the experimental data, while the red curves are calculated based on the model explained in the main text. Nuclear Bragg peaks causing artifacts in the magnetic signal are indicated with a subscript N. Figure provided by Dr. Frandsen.

is unrealistic considering the statistical noise in the data and the leakage from large (111) nuclear Bragg peak located around 2.8 Å^{-1}, which is about 60 times stronger than the magnetic scattering. Nevertheless, the presence of diffuse features in the spin-flip channel is sufficient to confirm that short-range AFM correlations survive above T_N, as expected from the mPDF analysis.

4.2.3 Muon spin relaxation

As an independent verification of the local magnetic properties of (Sr,Ba)MnO_3 revealed by neutron scattering, we performed μSR measurements on $Sr_{0.55}Ba_{0.45}MnO_3$ and $Sr_{0.4}Ba_{0.6}Mn_{0.95}Ti_{0.05}O_3$. Asymmetry spectra collected at various temperatures across the antiferromagnetic transition are shown for $Sr_{0.4}Ba_{0.6}Mn_{0.95}Ti_{0.05}O_3$ in Fig. 4.13(a).

Above T_N, the asymmetry relaxes slowly, with a single exponentially decaying component. Below the transition, we observe a fast front-end relaxation and a slower long-time component with amplitude about one-third the initial asymmetry amplitude of $\sim$0.24, as expected for magnetically ordered powder samples. The transition region is evident between 148 and 156 K for $Sr_{0.4}Ba_{0.6}Mn_{0.95}Ti_{0.05}O_3$ in Fig. 4.13(a), close to the transition temperature of 149 K observed from magnetometry measurements performed on the sample. Close inspection of the spectra shows that the relaxation in the paramagnetic state becomes more rapid as the temperature approaches T_N from above. This is a signature of critical spin dynamics near the transition, consistent with the development of short-range magnetic correlations observed by mPDF and polarized neutron scattering. The asymmetry spectra for $Sr_{0.55}Ba_{0.45}MnO_3$ likewise confirm a bulk magnetic transition at 195 K and show the same dynamic behavior just above T_N.

We analyzed the μSR data more quantitatively by performing fits to the asymmetry spectra using the program BEAMS [64]. We modeled the data using a sum of two exponential components, one for the fast front end and the other for the slower, long-time relaxation. The total initial amplitude of the two components was constrained to be equal to a constant representing the total initial asymmetry determined by a global fit to all the spectra, found to be 0.2390(3) for $Sr_{0.55}Ba_{0.45}MnO_3$ and 0.2356(4) for $Sr_{0.4}Ba_{0.6}Mn_{0.95}Ti_{0.05}O_3$. Above T_N, the fast front-end component was fixed to zero amplitude. The fast and slow relaxation rates, labeled λ_1 and λ_2, respectively, are shown in Fig. 4.13(b) and (c). λ_1 is proportional to the static field at the muon site [66] and therefore serves as an order parameter for the magnetic transition, revealing a rather continuous evolution of the static field for the two samples, as seen in Fig. 4.13(b). The slower rate λ_2 is related to the magnetic fluctuations [66]. The slight but observable increase in λ_2 as the temperature approaches T_N from above confirms the development of short-range magnetic correlations mentioned previously. The broad peak in λ_2 below T_N is evidence of critical spin dynamics, with the decrease at lower temperature caused by the freezing out of magnetic excitations.

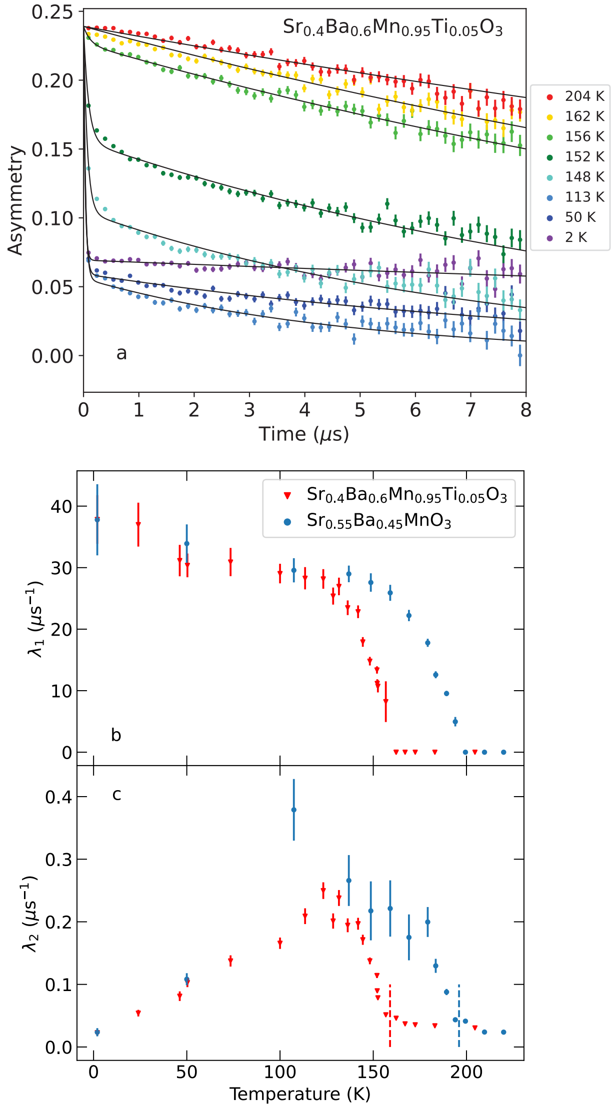

Figure 4.13 (a) μSR time spectra for $Sr_{0.4}Ba_{0.6}Mn_{0.95}Ti_{0.05}O_3$ at various temperatures above and below T_N. The colored symbols show the data, and the black curves are fits described in the main text. (b) Temperature-dependent relaxation rate corresponding to the fast front end of the asymmetry spectra for the samples with $(x, y) = (0.45, 0)$ and (0.6, 0.05), extracted from least-squares fits. (c) Same as for (b), but showing the relaxation rate corresponding to the long-time tail of the asymmetry spectra. The dashed vertical lines indicate T_N for the corresponding sample. Modelling performed by Christiana Zaugg.

Chapter 5

Discussion and Conclusion

5.1 Discussion

Based on the total scattering, polarized neutron scattering, and μSR data presented here, the local electronic environment in (Sr,Ba)(Mn,Ti)O_3 is characterized by widespread local symmetry breaking. This includes not only short-range tetragonal distortions resulting in local electric dipole formation deep into the high-temperature paraelectric phase, but also short-range AFM correlations that survive well above T_N. The occurrence of local symmetry breaking above ferroelectric or magnetic transitions is by no means unique or even particularly uncommon, but these observations nevertheless confirm the relevance of such behavior for (Sr,Ba)(Mn,Ti)O_3 and possibly other multiferroic systems, where local symmetry breaking has received mostly limited attention in the past.

Considering the behavior of the local atomic and magnetic structure together allows us to interrogate the coupling between the electric and magnetic degrees of freedom, a central issue for magnetoelectric multiferroics. To facilitate this, we plot in Fig. 5.1(a) the magnitude of the tetragonal distortion $c/a-1$ in $\mathrm{Sr_{0.4}Ba_{0.6}Mn_{0.95}Ti_{0.05}O_3}$ as a function of temperature for a short

PDF fitting range, together with the local magnetic order parameter obtained from the mPDF fits. We notice, once again, curvature returning the tetragonal structure towards a cubic structure, at temperatures above T_N. An issue not fully resolved in previous studies is the reason for the reduction of the tetragonal distortion upon approaching the AFM transition from above, beginning around 250 K in $Sr_{0.4}Ba_{0.6}Mn_{0.95}Ti_{0.05}O_3$. Here, it is clear that this reduction coincides precisely with the onset of short-range AFM correlations above T_N, providing direct evidence that the magnetic fluctuations are responsible for the reduced tetragonal distortion.

To illustrate this further, we plot the tetragonal distortion against the local magnetic order parameter in Fig. 5.1(b). The relationship can be well described by a line with slope -0.0037(1) μ_B^{-1}, demonstrating spontaneous linear magnetoelectric coupling in (Sr,Ba)(Mn,Ti)O_3. We emphasize that this linear relationship extends even to the short-range magnetic correlations above T_N, confirming that short-range correlations can facilitate the magnetoelectric coupling characteristic of the multiferroic phase. This coupling could be achieved either directly through interactions between the electric dipoles and the fluctuating spins or indirectly via magnetostructural coupling, by which the magnetic correlations drive a response in the structure, which then in turn influences the magnitude of the ferroelectric distortion. Further investigation, including theoretical work to model the microscopic interactions in (Sr,Ba)(Mn,Ti)O_3, will likely be necessary to answer this question. An equivalent plot for $Sr_{0.55}Ba_{0.45}MnO_3$ is shown in Fig. 5.1(c). The same trend appears, although it is noisier due to the smaller structural distortion in $Sr_{0.55}Ba_{0.45}MnO_3$ and fewer temperature points for which data were collected.

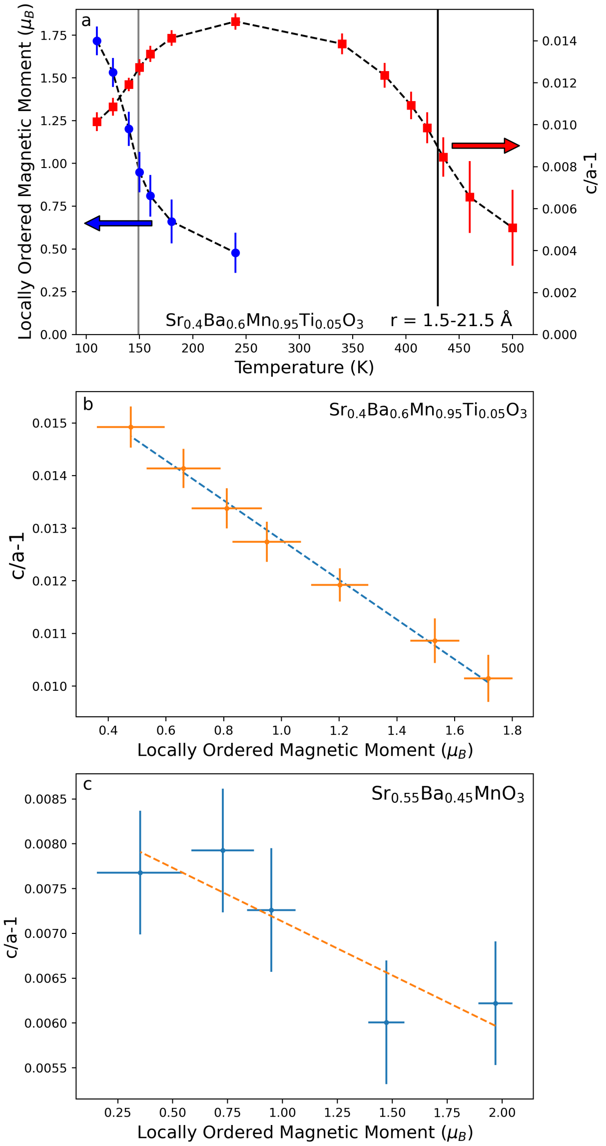

Figure 5.1 (a) Temperature dependence of the locally ordered magnetic moment for $\mathrm{Sr_{0.4}Ba_{0.6}Mn_{0.95}Ti_{0.05}O_3}$ (left vertical axis) and the tetragonal distortion $c/a-1$ for fitting range of $1.5-21.5$ Å (right vertical axis). (b) Tetragonal distortion versus local magnetic order parameter, highlighting spontaneous linear magnetoelectric coupling in the multiferroic state. (c) Similar linear magnetoelectric coupling for $\mathrm{Sr_{0.55}Ba_{0.45}MnO_3}$, but due to limited temperature experimentation, not as strong of a linear relationship is exhibited.

5.2 Conclusion

This thesis work has presented a comprehensive characterization of the local structural and magnetic behaviors in $Sr_{1-x}Ba_xMnO_3$. As a Type-I multiferroic that possesses unusually strong coupling between the ferroelectric and antiferromagnetic orders, this material has been established as a potential system for technological application and merits further inquiry into its characteristic behavior. The analysis of its local atomic and magnetic structure revealed local tetragonal distortions and short-range magnetic correlations above the respective structural and magnetic phase transitions.

Beginning with the atomic PDF data, the initial model-free analysis revealed abrupt changes in the PDF data at large r ranges, representative of the long-range phase transition; however, at a local level, the data showed very little change as temperature changed. This indicates that the symmetry breaking associated with the long-range structural transition is already present in the local structural environment above the transition temperature, highlighting the differences between the local and average scale structural behavior.

The Pearson correlation coefficient was used to quantify the similarity between two data sets at various temperatures and r ranges. This analysis confirmed the abrupt changes at the transition temperature in the long-range data, while the temperature evolution of the local structure was much more gradual. This again supports the conclusion that the local structure is characterized by broken local symmetry well above the ferroelectric transition temperature.

Modeling the PDF data with diffpy and PDFgui allowed us to describe the local structure more quantitatively. By performing boxcar fits, the a and c lattice parameters were extracted at various r ranges and temperatures. The long-range fits showed the expected behavior consistent with the average crystallographic structure, with a sharp structural transition signaling the onset of the ferroelectric order and a reduction of the tetragonal distortion below the antiferromagnetic transition. Locally, we saw tetragonal distortions above the Curie temperature, while an enhancement of ferroelectric distortions can be seen below the Néel temperature.

Analysis of the magnetic structure via mPDf revealed a build-up in short range magnetic correlations above T_N. When compared with the temperature dependence of the a and c lattice parameters, we observe that the lattice parameter values begin to approach each other above T_N around the temperature where the short-range magnetic correlations develop. Polarized neutron scattering measurements verified the nature and temperature dependence of the short-range magnetic correlations, as did muon spin spectroscopy.

Comparing the local magnetic order parameter to the tetragonal distortion confirmed that the development of short-range magnetic correlations coincides with the reduction of the tetragonal distortion, which can be considered a manifestation of the multiferroic coupling in $Sr_{1-x}Ba_xMnO_3$. The tetragonal distortion is reduced in linear proportion to the local magnetic order parameter. Perhaps the most significant finding of this study is that the reduction of the tetragonal distortion in the long-range, average crystallographic structure is initially driven by short-range, local magnetic correlations that develop in the paramagnetic state.

We note that the phenomenon of short-range magnetism driving long-range changes in the average structure, such as that seen in $(Sr,Ba)(Mn,Ti)O_3$, has also been observed in a diversity of other systems, such as a geometrically frustrated magnet [38] and a giant magnetostrictive material [42]. More generally, these results highlight a recurring theme in complex materials with intertwined orders: focusing only on the average, long-range behavior of the relevant degrees of freedom (e.g. lattice, charge, and spin) may result in an incomplete view of the system. Deeper understanding often requires careful study of the short-range, local correlations within and between these degrees of freedom, as revealed by local probes such as PDF and μSR used here.

Such methods of study of other materials, such as the aforementioned type-II multiferroic, $TbMnO_3$, will reveal more on the coupling mechanisms between magnetic and electric ordering. Further work for a strongly coupling type-I multiferroic $YMnO_3$ will also lead to a thorough comparison between type-I and type-II multiferroics. By analysis of two similar, yet fundamentally differing, multiferroic materials, we can gain a deeper understanding of multiferroic coupling and make progress toward designing more effective materials for future applications.

Bibliography

[1] B. Dabrowski, "Multiferroics for Detection of Magnetic and Electric Fields," In *Advanced Nanomaterials for Detection of CBRN*, J. Bonča and S. Kruchinin, eds., pp. 75–83 (Springer Netherlands, Dordrecht, 2020).

[2] N. A. Spaldin, "Multiferroics: Past, present, and future," MRS Bulletin **42,** 385–390 (2017), publisher: Cambridge University Press.

[3] M. Fiebig, T. Lottermoser, D. Meier, and M. Trassin, "The evolution of multiferroics," Nat. Rev. Mater. **1,** 16046 (2016).

[4] M. M. Vopson, "Fundamentals of Multiferroic Materials and Their Possible Applications," Crit. Rev. Solid State Mater. Sci. **40,** 223–250 (2015).

[5] H. Schmid, "Multi-ferroic magnetoelectrics," Ferroelectrics **162,** 317–338 (1994).

[6] N. A. Hill, "Why are there so few magnetic ferroelectrics?," The journal of physical chemistry B (2000)).

[7] S.-W. Cheong and M. Mostovoy, "Multiferroics: a magnetic twist for ferroelectricity," Nature Mater. **6,** 13–20 (2007).

[8] H. Sakai *et al.*, "Displacement-Type Ferroelectricity with Off-Center Magnetic Ions in Perovskite $Sr_{1-x}Ba_xMnO_3$," Phys. Rev. Lett. **107,** 137601 (2011).

[9] N. Spaldin and R. Ramesh, “Advances in magnetoelectric multiferroics,” Nature Mater. **18,** 203–212 (2019).

[10] O. Chmaissem, B. Dabrowski, S. Kolesnik, J. Mais, D. E. Brown, R. Kruk, P. Prior, B. Pyles, and J. D. Jorgensen, “Relationship between structural parameters and the Néel temperature in $\mathrm{Sr}_{1-x}\mathrm{Ca}_x\mathrm{MnO}_3$ ($0 <\sim x <\sim 1$) and $\mathrm{Sr}_{1-y}\mathrm{Ba}_y\mathrm{MnO}_3$ ($y <\sim 0.2$),” Phys. Rev. B **64,** 134412 (2001).

[11] D. K. Pratt, J. W. Lynn, J. Mais, O. Chmaissem, D. E. Brown, S. Kolesnik, and B. Dabrowski, “Neutron scattering studies of the ferroelectric distortion and spin dynamics in the type-1 multiferroic perovskite $\mathrm{Sr}_{0.56}\mathrm{Ba}_{0.44}\mathrm{MnO}_3$,” Phys. Rev. B **90,** 140401 (2014).

[12] V. Goian *et al.*, “Spectroscopic studies of the ferroelectric and magnetic phase transitions in multiferroic $\mathrm{Sr}_{1x}\mathrm{Ba}_x\mathrm{MnO}_3$,” J. Phys.: Condens. Mat. **28,** 175901 (2016).

[13] H. Somaily, S. Kolesnik, J. Mais, D. Brown, K. Chapagain, B. Dabrowski, and O. Chmaissem, “Strain-induced tetragonal distortions and multiferroic properties in polycrystalline $\mathrm{Sr}_{1-x}\mathrm{Ba}_x\mathrm{Mn}_{1-y}\mathrm{Ti}_y\mathrm{O}_3$ perovskites,” Phys. Rev. Materials **2,** 054408 (2018).

[14] K. Chapagain *et al.*, “Tunable multiferroic order parameters in $\mathrm{Sr}_{1-x}\mathrm{Ba}_x\mathrm{Mn}_{1-y}\mathrm{Ti}_y\mathrm{O}_3$,” Phys. Rev. Materials **3,** 084401 (2019).

[15] K. Momma and F. Izumi, “VESTA 3 for three-dimensional visualization of crystal, volumetric and morphology data,” J. Appl. Crystallogr. **44,** 1272–1276 (2011).

[16] G. H. Kwei, S. J. L. Billinge, S.-W. Cheong, and J. G. Saxton, “Pair-distribution functions of ferroelectric perovskites: direct observation of structural gound-states,” Ferroelectrics **164,** 57 (1995).

[17] T.Egami, “Local Structure of Ferroelectric Materials,” Annu. Rev. Mater. Res. **37,** 297–315 (2007).

[18] D. Hou, C. Zhao, A. R. Paterson, S. Li, and J. L. Jones, “Local structures of perovskite dielectrics and ferroelectrics via pair distribution function analyses,” J. Eur. Ceram. Soc. **38,** 971–987 (2018).

[19] F. Li, S. Zhang, D. Damjanovic, L.-Q. Chen, and T. R. Shrout, “Local Structural Heterogeneity and Electromechanical Responses of Ferroelectrics: Learning from Relaxor Ferroelectrics,” Adv. Funct. Mater. **28,** 1801504 (2018).

[20] Y. Yoneda, “Nanoscale structural analysis of ferroelectrics using pair distribution function,” JSAP Rev. **2023,** 230202 (2023).

[21] T. Egami and S. J. L. Billinge, *Underneath the Bragg peaks: structural analysis of complex materials*, 2nd ed. (Elsevier, Amsterdam, 2012).

[22] C. A. Young and A. L. Goodwin, “Applications of pair distribution function methods to contemporary problems in materials chemistry,” J. Mater. Chem. **21,** 6464–6476 (2011).

[23] H. Zhu, Y. Huang, J. Ren, B. Zhang, Y. Ke, A. K.-Y. Jen, Q. Zhang, X.-L. Wang, and Q. Liu, “Bridging Structural Inhomogeneity to Functionality: Pair Distribution Function Methods for Functional Materials Development,” Adv. Sci. **8,** 2003534 (2021).

[24] D. O. Akamo, A. O. Ijaola, T. T. George, K. Page, D. J. Keffer, Y. Li, M. Goswami, T. J. LaClair, K. Gluesenkamp, and O. Rios, “Bibliometric review and recent advances in total scattering pair distribution function analysis: 21 years in retrospect,” Eur. J. Mater. **0,** 1–35 (2022).

[25] S. J. L. Billinge, figures of a previous presentation (unpublished).

[26] B. A. Frandsen, figures of a previous presentation (unpublished).

[27] K. Kodama, S. Iikubo, S.-i. Shamoto, A. A. Belik, and E. Takayama-Muromachi, “Local Crystal Structure of Multiferroic System $BiMnO_3$ by Atomic Pair Distribution Function Analysis,” J. Phys. Soc. Jpn **76,** 124605 (2007).

[28] I.-K. Jeong, J. S. Ahn, B. G. Kim, S. Yoon, S. P. Singh, and D. Pandey, “Short- and medium-range structure of multiferroic $Pb(Fe_{1/2}Nb_{1/2})O_3$ studied using neutron total scattering analysis,” Phys. Rev. B **83,** 064108 (2011).

[29] S. Tripathi, V. Petkov, S. M. Selbach, K. Bergum, M.-A. Einarsrud, T. Grande, and Y. Ren, “Structural coherence and ferroelectric order in nanosized multiferroic $YMnO_3$,” Phys. Rev. B **86,** 094101 (2012).

[30] H. Sim, D. C. Peets, S. Lee, S. Lee, T. Kamiyama, K. Ikeda, T. Otomo, S.-W. Cheong, and J.-G. Park, “High-resolution structure studies and magnetoelectric coupling of relaxor multiferroic $Pb(Fe_{0.5}Nb_{0.5})O_3$,” Phys. Rev. B **90,** 214438 (2014).

[31] B. Jiang and S. M. Selbach, “Local and average structure of Mn- and La-substituted BiFeO3,” J. Solid State Chem. **250,** 75 – 82 (2017).

[32] S. H. Skjærvø, Q. N. Meier, M. Feygenson, N. A. Spaldin, S. J. L. Billinge, E. S. Bozin, and S. M. Selbach, “Unconventional Continuous Structural Disorder at the Order-Disorder Phase Transition in the Hexagonal Manganites,” Phys. Rev. X **9,** 031001 (2019).

[33] B. A. Frandsen, X. Yang, and S. J. L. Billinge, “Magnetic pair distribution function analysis of local magnetic correlations,” Acta Crystallogr. A **70,** 3–11 (2014).

[34] B. A. Frandsen and S. J. L. Billinge, “Magnetic structure determination from the magnetic pair distribution function (mPDF): ground state of MnO,” Acta Crystallogr. A **71,** 325–334 (2015).

[35] B. A. Frandsen, M. Brunelli, K. Page, Y. J. Uemura, J. B. Staunton, and S. J. L. Billinge, "Verification of Anderson Superexchange in MnO via Magnetic Pair Distribution Function Analysis and *ab initio* Theory," Phys. Rev. Lett. **116,** 197204 (2016).

[36] B. A. Frandsen, Z. Gong, M. W. Terban, S. Banerjee, B. Chen, C. Jin, M. Feygenson, Y. J. Uemura, and S. J. L. Billinge, "Local atomic and magnetic structure of dilute magnetic semiconductor (Ba,K)(Zn,Mn)$_2$As$_2$," Phys. Rev. B **94,** 094102 (2016), selected as Editors' Suggestion.

[37] B. A. Frandsen, K. A. Ross, J. W. Krizan, G. J. Nilsen, A. R. Wildes, R. J. Cava, R. J. Birgeneau, and S. J. L. Billinge, "Real-space investigation of short-range magnetic correlations in fluoride pyrochlores NaCaCo$_2$F$_7$ and NaSrCo$_2$F$_7$ with magnetic pair distribution function analysis," Phys. Rev. Materials **1,** 074412 (2017).

[38] B. A. Frandsen, E. S. Bozin, E. Aza, A. F. Martínez, M. Feygenson, K. Page, and A. Lappas, "Nanoscale degeneracy lifting in a geometrically frustrated antiferromagnet," Phys. Rev. B **101,** 024423 (2020).

[39] E. R. A. Fletcher, K. Higashi, Y. Kalcheim, H. Kageyama, and B. A. Frandsen, "Uniform structural phase transition in V$_2$O$_3$ without short-range distortions of the local structure," Phys. Rev. B **104,** 184115 (2021).

[40] H. L. Andersen, B. A. Frandsen, H. P. Gunnlaugsson, M. R. V. Jørgensen, S. J. L. Billinge, K. M. Ø. Jensen, and M. Christensen, "Local and long-range atomic/magnetic structure of non-stoichiometric spinel iron oxide nanocrystallites," IUCrJ **8,** 33–45 (2021).

[41] R. Baral *et al.*, "Real-space visualization of short-range antiferromagnetic correlations in a magnetically enhanced thermoelectric," Matter **5,** 1853–1864 (2022).

[42] R. Baral, A. M. Abeykoon, B. J. Campbell, and B. A. Frandsen, "Giant Spontaneous Magnetostriction in MnTe Driven by a Novel Magnetostructural Coupling Mechanism," Adv. Funct. Mater. p. 2305247 .

[43] J. Finney, "The complementary use of X-ray and neutron diffraction in the study of crystals," Acta Crystallographica Section B: Structural Science **51,** 447–467 (1995).

[44] S. H. Simon, *The Oxford Solid State Basics* (Oxford University Press, 2013).

[45] S. J. Billinge, S. H. Skjaervoe, M. W. Terban, S. Tao, L. Yang, Y. Rakita, and B. A. Frandsen, "Local structure determination using total scattering data," in *Comprehensive Inorganic Chemistry III, Third Edition* (Elsevier, 2023), pp. 222–247.

[46] G. Ehlers, J. R. Stewart, A. R. Wildes, P. P. Deen, and K. H. Andersen, "Generalization of the classical xyz-polarization analysis technique to out-of-plane and inelastic scattering," Rev. Sci. Instrum. **84,** 093901 (2013).

[47] O. Schärpf and H. Capellmann, "The XYZ-Difference Method with Polarized Neutrons and the Separation of Coherent, Spin Incoherent, and Magnetic Scattering Cross Sections in a Multidetector," Phys. Status Solidi A **135,** 359–379 (1993).

[48] J. R. Stewart, P. P. Deen, K. H. Andersen, H. Schober, J.-F. Barthelemy, J. M. Hillier, A. P. Murani, T. Hayes, and B. Lindenau, "Disordered materials studied using neutron polarization analysis on the multi-detector spectrometer, D7," J. Appl. Crystallogr. **42,** 69–84 (2009).

[49] S. J. Blundell, "Spin-polarized muons in condensed matter physics," Contemporary Physics **40,** 175–192 (2010).

[50] J. E. Sonier, "Muon Spin Rotation/Relaxation," (2002).

[51] A. D. Hillier *et al.*, "Muon spin spectroscopy," Nat. Rev. Methods Primers **2,** 4 (2022).

[52] "Pair Distribution Function," https://www.bnl.gov/nsls2/beamlines/beamline.php?r=28-ID-1 (Accessed October 15, 2023).

[53] J. Neuefeind, M. Feygenson, J. Carruth, R. Hoffmann, and K. K. Chipley, "The Nanoscale Ordered MAterials Diffractometer NOMAD at the Spallation Neutron Source SNS," Nucl. Instrum. Meth. B **287,** 68 – 75 (2012).

[54] "Muon Beamlines," https://cmms.triumf.ca/equip/muSRbeamlines.html (Accessed October 15, 2023).

[55] I. A. Zaliznyak, A. T. Savici, V. O. Garlea, B. Winn, U. Filges, J. Schneeloch, J. M. Tranquada, G. Gu, A. Wang, and C. Petrovic, "Polarized neutron scattering on HYSPEC: the HYbrid SPECtrometer at SNS," J. Phys.: Conf. Ser. **862,** 012030 (2017).

[56] "Spallation Neutron Source," https://neutrons.ornl.gov/sns (Accessed October 15, 2023).

[57] B. H. Toby and R. B. Von Dreele, "*GSAS-II*: the genesis of a modern open-source all purpose crystallography software package," J. Appl. Crystallogr. **46,** 544–549 (2013).

[58] M. McDonnell, D. Olds, K. Page, J. Neuefeind, M. Tucker, J. Bilheux, W. Zhou, and P. Peterson, "ADDIE: ADvanced DIffraction Environment – A Software Environment for Analyzing Neutron Diffraction Data," Acta Crystallogr. A **73,** a377 (2017).

[59] J. Kieffer and D. Karkoulis, "PyFAI, a versatile library for azimuthal regrouping," J. Phys.: Conf. Ser. SRI2012 (2013).

[60] X. Yang, P. Juhás, C. Farrow, and S. J. L. Billinge, "xPDFsuite: an end-to-end software solution for high throughput pair distribution function transformation, visualization and analysis," arXiv (2015), 1402.3163.

[61] C. L. Farrow, P. Juhás, J. Liu, D. Bryndin, E. S. Božin, J. Bloch, T. Proffen, and S. J. L. Billinge, “PDFfit2 and PDFgui: Computer programs for studying nanostructure in crystals,” J. Phys.: Condens. Mat. **19,** 335219 (2007).

[62] B. A. Frandsen, H. K. Parker, J. A. Christensen, E. Stubben, and S. J. L. Billinge, “diffpy.mpdf: open-source software for magnetic pair distribution function analysis,” J. Appl. Crystallogr. **55,** 1377—1382 (2022).

[63] A. T. Savici, I. A. Zaliznyak, V. O. Garlea, and B. Winn, “Data processing workflow for time of flight polarized neutrons inelastic measurements,” J. Phys.: Conf. Ser. **862,** 012023 (2017).

[64] K. A. Petersen, J. Black, and B. A. Frandsen, “BEAMS: Basic and Effective Analysis for Muon spin Spectroscopy,” p. https://github.com/FrandsenGroup/beams (2021).

[65] B. J. Campbell, H. T. Stokes, J. M. Perez-Mato, and J. Rodríguez-Carvajal, “Introducing a unified magnetic space-group symbol,” Acta Crystallographica Section A: Foundations and Advances **78,** 99–106 (2022).

[66] Y. Uemura, “μSR relaxation functions in magnetic materials,” in *Muon Science: Muons in Physics, Chemistry and Materials*, S. Lee, R. Cywinski, and S. Kilcoyne, eds., (Taylor & Francis, New York, 1999).